The Astrophysical Journal, 1011:172 (24pp), 2026 November 10 https://doi.org/10.3847/1538-4357/aea6b5
© 2026. The Author(s). Published by the American Astronomical Society.
OPEN ACCESS

Where Galaxies Go to Die: The Environments of Massive Quiescent Galaxies at $3 < z < 5$

Ian McConachie[1,2], Anna de Graaff[3], Michael V. Maseda[1], Joel Leja[4,5,6], Yunchong Zhang[7], David J. Setton[8,9,30], Rachel Bezanson[7], Leindert A. Boogaard[10], Gabriel Brammer[11,12], Nikko J. Cleri[4,5,6], Olivia R. Cooper[13,29], Karl Glazebrook[14], Rashmi Gottumukkala[11,15], Jenny E. Greene[8], Andy D. Goulding[8], Michaela Hirschmann[16], Gourav Khullar[17,18], Ivo Labbe[19], Zach Lewis[1], Jorryt Matthee[20], Tim B. Miller[21], Rohan P. Naidu[22,23,30], Themiya Nanayakkara[19], Erica J. Nelson[13], Pascal A. Oesch[11,12,24], Sedona H. Price[7,25], Katherine A. Suess[13], Bingjie Wang[26,30], Katherine E. Whitaker[11,27], and Christina C. Williams[28]

[1] Department of Astronomy, University of Wisconsin–Madison, 475 N. Charter St., Madison, WI 53706, USA; imcconachie@carnegiescience.edu
[2] Observatories of the Carnegie Institution for Science, 813 Santa Barbara Street, Pasadena, CA 91101, USA
[3] Max-Planck-Institut für Astronomie, Königstuhl 17, D-69117 Heidelberg, Germany
[4] Department of Astronomy & Astrophysics, The Pennsylvania State University, University Park, PA 16802, USA
[5] Institute for Computational & Data Sciences, The Pennsylvania State University, University Park, PA 16802, USA
[6] Institute for Gravitation and the Cosmos, The Pennsylvania State University, University Park, PA 16802, USA
[7] Department of Physics and Astronomy and PITT PACC, University of Pittsburgh, Pittsburgh, PA 15260, USA
[8] Department of Astrophysical Sciences, Princeton University, 4 Ivy Lane, Princeton, NJ 08544, USA
[9] The William H. Miller III Department of Physics and Astronomy, The Johns Hopkins University, Baltimore, MD 21218, USA
[10] Leiden Observatory, Leiden University, PO Box 9513, NL-2300 RA Leiden, The Netherlands
[11] Cosmic Dawn Center (DAWN), Denmark
[12] Niels Bohr Institute, University of Copenhagen, Jagtvej 128, København N, DK-2200, Denmark
[13] Department for Astrophysical & Planetary Science, University of Colorado, Boulder, CO 80309, USA
[14] Centre for Astrophysics and Supercomputing, Swinburne University of Technology, PO Box 218, Hawthorn, VIC 3122, Australia
[15] Niels Bohr Institute, University of Copenhagen, Jagtvej 128, Copenhagen, Denmark
[16] Institute of Physics, Laboratory for Galaxy Evolution, EPFL, Observatory of Sauverny, Chemin Pegasi 51, CH-1290 Versoix, Switzerland
[17] Department of Astronomy, University of Washington, Physics-Astronomy Building, Box 351580, Seattle, WA 98195-1700, USA
[18] eScience Institute, University of Washington, Physics-Astronomy Building, Box 351580, Seattle, WA 98195-1700, USA
[19] Centre for Astrophysics and Supercomputing, Swinburne University of Technology, Melbourne, VIC 3122, Australia
[20] Institute of Science and Technology Austria (ISTA), Am Campus 1, 3400 Klosterneuburg, Austria
[21] Center for Interdisciplinary Exploration and Research in Astrophysics (CIERA), Northwestern University, 1800 Sherman Ave, Evanston, IL 60201, USA
[22] MIT Kavli Institute for Astrophysics and Space Research, Cambridge, MA 02139, USA
[23] Institute for Astronomy, University of Hawai'i, 2680 Woodlawn Drive, Honolulu, HI 96822, USA
[24] Department of Astronomy, University of Geneva, Chemin Pegasi 51, 1290 Versoix, Switzerland
[25] Space Telescope Science Institute, 3700 San Martin Drive, Baltimore, MD 21218, USA
[26] Department of Astrophysical Sciences, Princeton University, Princeton, NJ 08544, USA
[27] Department of Astronomy, University of Massachusetts, Amherst, MA 01003, USA
[28] NSF National Optical-Infrared Astronomy Research Laboratory, 950 North Cherry Avenue, Tucson, AZ 85719, USA
Received 2025 October 28; revised 2026 June 29; accepted 2026 August 7; published 2026 November 2

Abstract

At low redshift, massive quiescent galaxies (MQGs) are most frequently found in massive, rich galaxy clusters, but at high redshift the trend is less clear. Here, we present spectroscopic evidence of the effects of environment on the formation and assembly of high-redshift MQGs. We identify 26 (9) $\log(M_*/M_\odot) \geqslant 10.5$ ($10.0 \leqslant \log(M_*/M_\odot) < 10.5$) spectroscopically confirmed quiescent galaxies in the UDS and EGS fields at $3 < z < 5$ with NIRSpec spectroscopy from the Red Unknowns: Bright Infrared Extragalactic Spectroscopic (RUBIES) survey and other public JWST programs. We measure the density contrast in these fields by applying a Monte Carlo Voronoi tessellation density-mapping technique to photometric and spectroscopic redshifts of $m_{\rm F444W} < 27.5$ sources. We robustly detect 19 massive overdense peaks with $\log(M_{\rm Peak}/M_\odot) \geqslant 13$ and seven extended massive protoclusters ($\log(M_{\rm Struct}/M_\odot) \geqslant 13.85$). We observe that MQGs are preferentially found in these massive peaks and within these massive structures: ≈50% of MQGs are found in massive peaks, compared to ≈25% of massive star-forming galaxies (MSFGs), and quiescent fractions are higher in these regions than in the coeval field. We show that when all stellar mass is assumed to form in situ, the inferred masses of MQG progenitors are significantly higher than those of high-z massive galaxies in observations or simulations. Accounting for ex situ star formation and scaling merger rates by the local galaxy overdensity significantly lessens this tension, which indicates that ex situ star formation plays a key role in MQG mass assembly in overdense environments.

[29] NSF Astronomy and Astrophysics Postdoctoral Fellow.
[30] NHFP Hubble Fellow.

Original content from this work may be used under the terms of the Creative Commons Attribution 4.0 licence. Any further distribution of this work must maintain attribution to the author(s) and the title of the work, journal citation and DOI.

Unified Astronomy Thesaurus concepts: Quenched galaxies (2016); Galaxy environments (2029); High-redshift galaxy clusters (2007); Galaxies (573)

Materials only available in the online version of record: animation, interactive figure

1. Introduction

The formation and evolution of massive quiescent galaxies (MQGs) at high redshift ($z > 3$) represent the extremes of the Universe. Though rare, their remarkable masses place them at the upper end of the galaxy stellar mass function (SMF; e.g., A. Muzzin et al. 2013; J. R. Weaver et al. 2023), necessitating strong active galactic nucleus (AGN) feedback in order to achieve a sustained period of quiescence (e.g., A. Man & S. Belli 2018; C. d. P. Lagos et al. 2024). The sensitivity of this population to the exact mechanism driving the cessation of star formation leads to a frustrating difficulty reproducing the observed number densities of quiescent galaxies at $z > 3$ (T. Nanayakkara et al. 2024; W. M. Baker et al. 2025a, 2025b; Y. Zhang et al. 2026a).

In the era of JWST, NIRSpec's high sensitivity has given access to the previously inaccessible stellar continua of the faintest and reddest of these sources, uncovering MQGs at higher redshifts (A. C. Carnall et al. 2023; A. C. Carnall et al. 2024; A. Weibel et al. 2024; A. de Graaff et al. 2025a) and with even older ages (K. Glazebrook et al. 2024; I. McConachie et al. 2026). These subsets of the MQG population come into conflict with theoretical models not only with their early deaths, but also by their even earlier births. Fitting the observed photometry and spectra to synthetic models of stars, gas, and dust assembled by sophisticated modeling tools often suggests that incredible amounts of mass formed at extremely early cosmic times, which, if formed and contained in a single dark matter halo, possibly conflicts with not only models of galaxy formation but also potentially with fundamental ΛCDM cosmology (P. Behroozi & J. Silk 2018; M. Boylan-Kolchin 2023).

But galaxies are social creatures, not strictly isolated systems; environment has been shown to play a critical role in a galaxy's evolution, leading to differences in galaxy properties like stellar mass and star formation between galaxies in overdense environments versus the coeval field. It is long established that the properties of galaxies are not solely intrinsic, but often strongly depend on their neighbors and environments (A. Dressler 1980). There is a clear bimodality in galaxy populations in the Universe today: early-type galaxies are quiescent, old, red, elliptical, and preferentially found in regions of high density, whereas late-type galaxies tend to be less massive, actively forming stars, younger, blue, have spiral morphologies, and live in lower-density environments. This leads to a clear relationship between a galaxy's local environment and its properties, e.g., star formation rate (SFR; S. L. McGee et al. 2011; A. R. Wetzel et al. 2012), stellar age (G. Kauffmann et al. 2003), color (I. Strateva et al. 2001; M. R. Blanton et al. 2003; I. K. Baldry et al. 2004; G. B. Brammer et al. 2009), and morphology (A. van der Wel et al. 2014), which is well understood and uncontroversial.

At higher redshifts, this bimodality breaks down, in no small part due to the nature of high-redshift ($z > 3$) environments. Insufficient time has passed for protoclusters (i.e., cluster progenitors) to virialize and relax, so they often lack the hot intracluster medium (ICM) with which clusters quench star formation (J. E. Gunn & I. G. J. Richard 1972; R. B. Larson et al. 1980; M. G. Abadi et al. 1999; M. L. Balogh & S. L. Morris 2000; M. L. Balogh et al. 2000). While particularly massive, rich, and mature protoclusters may sport a proto-ICM (L. D. Mascolo et al. 2023; M. Lepore et al. 2024), the hot gas in these structures is relatively low density and contained within a small subvolume within the structure—in other words, it cannot produce the widespread quenching seen in low-redshift clusters. Indeed, rather than the sites of quiescence, overdensities at high redshift are thought to be regions of vigorous, enhanced (not suppressed), star formation (e.g., B. C. Lemaux et al. 2022; P. Staab et al. 2024), fueled by inflows of pristine gas from the early cosmic web.

While the gas-rich nature of high-redshift overdensities allows for more in situ star formation, their high merger fractions provide an additional pathway for mass assembly (J. M. Lotz et al. 2013; N. K. Hine et al. 2016; C. Watson et al. 2019; S. Liu et al. 2023; T. Shibuya et al. 2025). At low redshifts, galaxies in the deep potential wells of virialized clusters have high velocity dispersions, which suppress galaxy–galaxy interactions (S. Alonso et al. 2012; H.-Y. Jian et al. 2012; K. C. Omori et al. 2023). Galaxies in high-redshift protoclusters, on the other hand, lack the velocity to overcome their gravitational attraction to each other. This turns what would have been low-redshift near misses into high-redshift certain collisions, leading to extreme starbursts and AGN (B. D. Lehmer et al. 2009; J. M. Lotz et al. 2013; N. K. Hine et al. 2016; S. Mei et al. 2023).

The high incidence of $z \gtrsim 3$ MQGs discovered in overdense structures (B. S. Kalita et al. 2021; M. Kubo et al. 2021; I. McConachie et al. 2022; K. Ito et al. 2023; T. Kakimoto et al. 2024; M. Tanaka et al. 2024; S. M. Urbano Stawinski et al. 2024a; A. de Graaff et al. 2025a; K. Ito et al. 2025; C. K. Jespersen et al. 2025; I. McConachie et al. 2026) or in close proximity to other massive galaxies (C. Schreiber et al. 2018; A. C. Carnall et al. 2024; C. Turner et al. 2025; L. Kawinwanichakij et al. 2026) suggests a link between early, rapid growth and early cosmic structure. Clearly, when considering the question *how* do high-redshift MQGs form and quench, it is therefore necessary to consider the question *where* do high-redshift MQGs form and quench.

In this work, we present a first systematic investigation of the environments of spectroscopically confirmed MQGs in the UDS and EGS fields. In Section 2, we provide an overview of the photometric and spectroscopic data used in this analysis. We present a set of spectroscopically confirmed massive (quiescent) galaxies in Section 3. Section 4 details the methods used to quantify environment in these fields and identify prominent protostructures. In Section 5, we show the link between MQGs' environments and evolution at $3 < z < 5$, and in Section 6 we discuss MQG assembly in the context of their environments. Our main conclusions are summarized in Section 7. Throughout, we assume a flat ΛCDM cosmology with $H_0 = 70 \mathrm{kms}^{-1}\mathrm{Mpc}^{-1}$, $\Omega_m = 0.3$, and $\Omega_\Lambda = 0.7$. We utilize a Chabrier initial mass function (G. Chabrier 2003) and we quote surviving stellar masses unless stated otherwise. All magnitudes are in the AB system (J. B. Oke & J. E. Gunn 1983).

2. Data

First, we describe the data used in the analyses. In our MQG modeling (Section 3), we match NIRSpec Micro-Shutter Assembly (MSA) multi-object spectroscopy to the photometric catalogs and model both the photometry and spectroscopy of F444W-bright sources. In the density mapping (Section 4), we match all JWST/NIRSpec MSA spectroscopy and archival spectroscopic catalogs to the photometric catalogs, using spectroscopic redshifts when available and photometric redshifts otherwise.

2.1. Photometric Catalogs

In this work, we use point-spread function (PSF)-matched photometric catalogs in the EGS (L. Wright et al. 2024) and UDS (S. E. Cutler et al. 2024) fields. The catalogs were created with Hubble Space Telescope (HST; F435W, F606W, F814W, F105W, F125W, F140W, and F160W) and NIRCam (F115W, F150W, F200W, F277W, F356W, F410M, and F444W) imaging from the CEERS (S. L. Finkelstein et al. 2024) and PRIMER (PRIMER also has F090W imaging; C. T. Donnan et al. 2024) programs. Mosaic images reduced with `grizli` (G. Brammer 2023a) were downloaded from the Dawn JWST Archive (DJA v7.2; F. Valentino et al. 2023). Sources were detected from a combined F277W–F356W–F444W noise-equalized image, and aperture photometry was extracted from the individual mosaics after they were degraded to F444W resolution. Circular apertures 0.″32, 0.″48, 0.″70, 1.″0, or 1.″4 in diameter were used, depending on isophotal area and the presence of nearby objects; the full process is detailed in J. R. Weaver et al. (2024).

2.1.1. Photometric Redshifts

We obtain photometric redshifts with the code `eazy` (G. B. Brammer et al. 2008). `eazy` matches synthetic template spectra created through linear combinations of empirical templates and finds the solution which best fits the observed photometry at every point along a redshift grid by minimizing χ^2. Because `eazy` calculates the χ^2 on this grid, it is then straightforward to recover a redshift probability distribution $p(z)$. We use this $p(z)$ (hereafter the "photometric $p(z)$") when statistically resampling redshifts in Section 4.

We use the updated template set `agn_blue_sfhz_13`, which contains 12 galaxy templates derived from the flexible stellar population synthesis (FSPS) models (C. Conroy et al. 2009; C. Conroy & J. E. Gunn 2010), an additional FSPS template made to match an extreme emission-line galaxy at $z = 8.5$ (`fsps_4590`), and a "Little Red Dot" template with extreme emission lines and a red optical spectrum (`j0647agn+torus`; M. Killi et al. 2024).

2.2. Spectroscopic Catalogs

The bulk of spectroscopy used in this work is sourced from the Red Unknowns: Bright Infrared Extragalactic Spectroscopic (RUBIES, GO #4233; A. de Graaff et al. 2025b) survey. The RUBIES survey observed 12 (6) JWST/NIRSpec MSA masks in the UDS (EGS) fields, obtaining spectroscopy in the NIRSpec PRISM and G395M grating. The RUBIES selection function highly weighted relatively rare red (in F150W − F444W) and bright (in F444W) high-redshift ($z_{\rm phot} > 3$) sources.

To maximize spectroscopic coverage, we further utilize legacy spectroscopic catalogs and all publicly available NIRSpec spectra on the DJA (G. Brammer 2023b; K. E. Heintz et al. 2024; A. de Graaff et al. 2025b) in the UDS and EGS fields. Arranged by program ID, we include spectra from JWST programs #1213, #1215 (GTO-WIDE; M. V. Maseda et al. 2024), #1345 (CEERS-ERS; S. L. Finkelstein et al. 2023, 2024), #2565 (T. Nanayakkara et al. 2024; T. Nanayakkara et al. 2025), #3543 (EXCELS; A. C. Carnall et al. 2024), #3567 (DEEPDIVE; K. Ito et al. 2026), #4106 (PI: E. Nelson), #4233 (RUBIES; A. de Graaff et al. 2025b), #4287 (M. Tang et al. 2025), #5224 (Mirage or Miracle; PIs: R. Naidu & P. Oesch), and #6368 (CAPERS; PI: M. Dickinson).

2.2.1. NIRSpec Spectroscopic Redshifts

We produce two lists of spectra, one for spectral energy distribution (SED) modeling (Section 3) and one for our density-mapping procedure (Section 4). In both cases, all spectra were taken from the DJA v4.4 (G. Brammer & F. Valentino 2025).[31] We require a robust redshift (grade = 3) for the spectrum to have a match within 0.″5 in our photometric catalogs and for that match to be detected in F444W. Of the 4823 unique $m_{\rm F444W} < 27.5$ matched sources, we visually examined slit placements on NIRCam mosaics for the 14 with $0.''3 < r_{\rm match} < 0.''5$. Twelve of these spectra are correctly paired with sources that are extended and/or significantly off-center in the MSA slitlet. The spectrum of one faint source at $z = 2.9$ in EGS is misidentified as a neighboring galaxy, and one $z = 4.8$ spectrum could be an extended source or a misidentification of a neighbor. These two failures in the catalog matching do not impact our results.

Spectra for spectrophotometric SED modeling. For this set, we select NIRSpec spectra of bright sources ($m_{\rm F444W} < 24.5$) with sufficiently high signal-to-noise ratio (S/N) and wavelength coverage in the rest-frame optical for spectrophotometric modeling with `Prospector`. We group DJA NIRSpec spectra by their associated unique source in the photometric catalogs. Sources identified as Little Red Dots in the literature (e.g., R. E. Hviding et al. 2025; A. de Graaff et al. 2026) are removed from the list and not modeled.

Spectra are then scored based on their summed S/N in the rest-frame optical ($\sum_\lambda F_\lambda / \sqrt{\sum_\lambda E_\lambda^2}$, where F and E are the flux and error spectra). We retain the spectrum with the highest summed S/N in each grating and filter combination. When medium- or high-resolution gratings overlap (e.g., G140M and G235M or G235M and G395M), we scale the spectra to equalize the flux in the overlapping region, degrade the resolution of the higher-resolution grating using `SpectRes` (A. C. Carnall 2017), and coadd the spectra in the overlap. The individual spectra used to produce the combined spectrum are replaced in the list by the combined spectrum, which receives its own summed S/N score. For each source, we retain the single spectrum with the highest score across all gratings and filters.

Finally, we flag and remove spectra that cover less than two-thirds of the rest-frame optical or have median S/N < 2.5 in the rest-frame optical. Unique sources which have spectroscopic redshifts but zero spectra for SED modeling as a result of this choice are added to a subcategory for photometry-only SED modeling in Section 3.3. After rejecting spectra with poor

[31] We manually add the custom reduction of the G235M spectrum for DeepDive-61167 from K. Ito et al. (2025) to the DJA catalogs.

rest-frame optical coverage or low S/N, we are left with 282 unique sources with NIRSpec spectra.

Spectra for density mapping. Here, the primary quantity we care about is the redshift and its uncertainty, so we rank spectra based on these quantities. For each spectrum, we remeasure the spectroscopic redshift with `msaexp` (G. Brammer 2023b), fitting the continuum with a 41-degree spline and the emission lines with Gaussians on a redshift grid. From the χ^2 values on the redshift grid, we obtain a spectroscopic $p(z)$ distribution for each `msaexp` spectral fit (as was done with the `eazy`χ^2 grid in Section 2.1.1), which we later use in Section B.1.2. In the case of sources with spectra from multiple programs, masks, or gratings, we select the spectrum with the highest redshift precision, which we define as $\delta_z = (z_{84} - z_{16})/(2(1 + z_{50}))$, where z_N is the Nth percentile of the spectroscopic $p(z)$ distribution. In this way, we select for narrower $p(z)$'s (i.e., typically grating spectra with emission lines when available). Overall, NIRSpec redshifts are generally reliable and our results are robust to this choice, even weighting PRISM spectra over grating spectra. Of the 5318 (4583) spectra in UDS (EGS), 2555 (2113) are unique sources.

2.2.2. Other Spectroscopy

Due to the wealth of legacy programs in these fields, we are able to supplement our list of spectra for density mapping with spectroscopic catalogs from the literature. We include the ground-based spectroscopic catalogs from the Deeper than DEEP survey (S. M. Urbano Stawinski et al. 2024b) in the EGS, VANDELS (B. Garilli et al. 2021) in the UDS, and MOSDEF (M. Kriek et al. 2015) in both fields, taking only redshifts flagged as robust (flags 3 and 4 in Deeper than DEEP and VANDELS; flags 5, 6, and 7 in MOSDEF). These ground-based catalogs feature abundant robust spectroscopic redshifts in the $3 < z < 5$ range to help fill in the gaps between NIRSpec pointing footprints. We incorporate the 3DHST catalog (R. E. Skelton et al. 2014; I. G. Momcheva et al. 2016) in our analyses for both fields. In addition to photometric redshifts and grism redshifts, the 3DHST catalog includes ground-based spectroscopic redshifts from the DEEP2/3 surveys (M. C. Cooper et al. 2007; J. A. Newman et al. 2013) in the EGS and redshifts from a heterogeneous set of small ground-based surveys in the UDS. While most redshifts in this catalog are at $z < 2$ and do not contribute directly to our $3 < z < 5$ sample, including them allows us to fix these sources to low redshift and prevent them from contaminating our high-redshift analyses. Sources with $m_{\rm F444W} < 24.5$ at $3 < z < 5$ that have spectroscopic redshifts from the ground-based/HST catalogs are added to the subset for photometric modeling in Section 3.3.

3. Massive Quiescent Galaxies

To assemble a larger sample of massive quiescent and massive star-forming galaxies (MSFGs), from the list of spectra from Section 2.2 we select all 282 galaxies with $m_{\rm F444W} \leqslant 24.5$ (0.5 mag fainter than the F444W magnitude limit used for the $2 < z < 5$ quiescent galaxy analysis in Y. Zhang et al. 2026a) and fit them with `Prospector`.

3.1. Spectrophotometric Prospector Modeling

We use the Bayesian inference package `Prospector` (J. Leja et al. 2017; B. D. Johnson et al. 2021) with the nested sampler `dynesty` (J. S. Speagle 2020) to simultaneously model the JWST/NIRSpec spectra and observed 0.3–5 μm HST and JWST photometry of all 282 galaxies with $m_{\rm F444W} \leqslant 24.5$ in the UDS and EGS fields.[32] We use the MILES spectral stellar library (P. Sanchez-Blazquez et al. 2006; J. Falcón-Barroso et al. 2011) and MIST isochrones (J. Choi et al. 2016; A. Dotter 2016). Below, we detail the parameters and priors of our model. All priors are uniform/flat unless stated otherwise. Redshift is fit in a narrow range $z_{\rm spec} \in [z_{\rm DJA} - 0.05, z_{\rm DJA} + 0.05]$, though in all cases we find excellent agreement between $z_{\rm spec}$ and $z_{\rm DJA}$. Though F444W-bright sources are expected to be preferentially more massive, we apply a wide prior to formed stellar mass, $\log(M_{*,\rm formed}/M_\odot) \in [7, 12]$. Metallicity is fit with a prior $\log(Z/Z_\odot) \in [-1, 0.19]$ (i.e., a logarithmic prior $Z \in [0.1, 1.5]$). For the parameterization of the model's star formation history (SFH), we choose to use the "continuity" SFH (J. Leja et al. 2019), which fits constant SFRs in n fixed user-defined bins. We use 10 bins, spaced thus: three young bins at [0, 10]Myr, [10, 50]Myr, and [50, 100] Myr (i.e., bins with widths of 10, 40, and 50 Myr) to recover recent star formation, followed by seven uniformly logarithmically spaced bins in lookback time until the Big Bang. The base continuity SFH utilizes a Student's t-distribution prior between neighboring SFH bins centered at $\Delta \log {\rm SFR} = 0$ with $\sigma = 0.3$ and $\nu = 2.0$. We parameterize extinction from dust with the M. Kriek & C. Conroy (2013) dust law with free optical depth $\tau_{\rm dust} \in [0, 6]$ and deviation from the D. Calzetti et al. (2000) dust law slope $\delta \in [-1, 0.4]$. We set attenuation around stars younger than 10 Myr to be twice that of older populations.

Because MQGs have been shown to frequently host AGN (e.g., L. Bugiani et al. 2025; K. Ito et al. 2026), we marginalize over nebular emission lines (i.e., we fit them with simple Gaussian profiles rather than tie emission to active star formation). When fitting medium- or high-resolution grating spectra, we mask the region around the Na I D doublet at 5861–5897 Å rest frame due to absorption from the interstellar medium. To flux-calibrate our spectra, we scale the spectrum to the model with a seven-degree Chebyshev polynomial at each likelihood call with the `PolySpecModel` procedure. To account for broadening from the NIRSpec gratings, we convolve our models with the JDOX resolution curve, which we multiply by a factor of 1.3 (A. de Graaff et al. 2024; M. Slob et al. 2024; T. Nanayakkara et al. 2024). We fit the velocity dispersion of stars and gas as two independent parameters, $\sigma_* \in [0, 1000]$ km s^{-1} and $\sigma_{\rm gas} \in [0, 1000]$ km s^{-1}. We include a spectroscopic outlier model: The uncertainties of a fraction of spectroscopic outlier data points $f_{\rm out} \in [10^{-5}, 0.2]$ are inflated by a factor of 5 to account for bad pixels and a mismatch between the model and spectra. We also fit a noise jitter term, $j_{\rm spec} \in [0.5, 3.0]$, as a factor multiplied to all spectroscopic uncertainties.

3.2. Identifying Massive Quiescent Galaxies

We show the sample of $3 < z < 5$ massive quiescent galaxies in Figure 1 with their observed spectra in black and maximum a posteriori (MAP) Prospector models in red. Y. Zhang et al. (2026a) showed that $m_{\rm F444W} < 24$ is mass

[32] We exclude F814W and F606W fluxes from the fit of RUBIES-EGS-QG1 due to the presence of a diffraction spike from a nearby star in HST Advanced Camera for Surveys imaging.

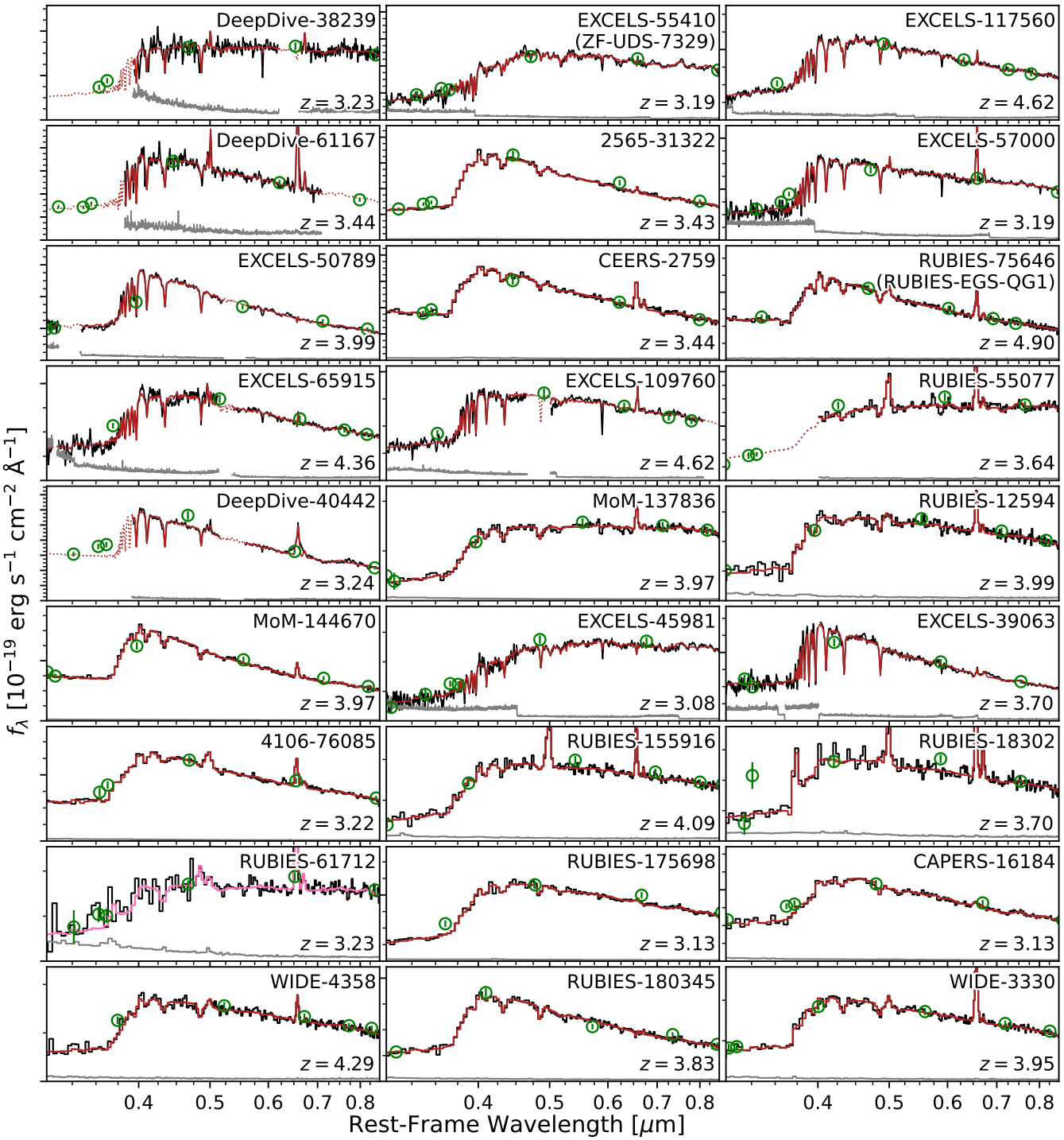


Figure 1. The 26 spectroscopically confirmed $\log(M_*/M_\odot) \geqslant 10.5$ quiescent galaxies with JWST spectroscopy that form our sample (and one marginally quiescent galaxy). Galaxies are shown in order of descending inferred stellar mass, left to right, top to bottom. In each panel, the NIRSpec spectrum and uncertainty are shown in black and gray with the MAP `Prospector` model spectrum overlaid in red (pink for the marginally quiescent galaxy). For visibility, we smooth the medium-resolution grating spectra and their models with a Gaussian filter. Green open circles with error bars show the photometry. To scale the observed, error, and model spectra to the observed photometry, the inverted calibration vector is applied. Each major (minor) tick along the vertical axis is $(0.25 \times)10^{-19}$ erg s^{-1}cm^{-2} Å^{-1}. In each panel, we give the spectrum ID and redshift (for other properties, see Table 1). Distinct sources with different names in the literature (e.g., K. Glazebrook et al. 2024; A. de Graaff et al. 2025a) have these names given in parentheses; we use them hereafter.

complete down to $\log(M_*/M_\odot) = 10.5$ for the quiescent galaxies in RUBIES. We adopt a limit 0.5 mag fainter than their "massive galaxy" mass cutoff for the analysis presented here (right panel in Figure 2). In Figure 3, we show how we classify galaxies as star-forming or quiescent based on their inferred properties. For each modeled galaxy, we sample the model's posterior 2000 times and take the median SFR$/M_*$ of the posterior to be the galaxy's specific star formation rate (sSFR). We require quiescent galaxies to have $\log(\mathrm{sSFR}/\mathrm{yr}^{-1}) < -10$ (using an alternative selection, e.g., $\mathrm{sSFR} < 0.2/t_{\mathrm{univ}}$ does not affect our results; top right of Figure 2). Galaxies with $\log(\mathrm{sSFR}_{16}/\mathrm{yr}^{-1}) < -10$ are labeled

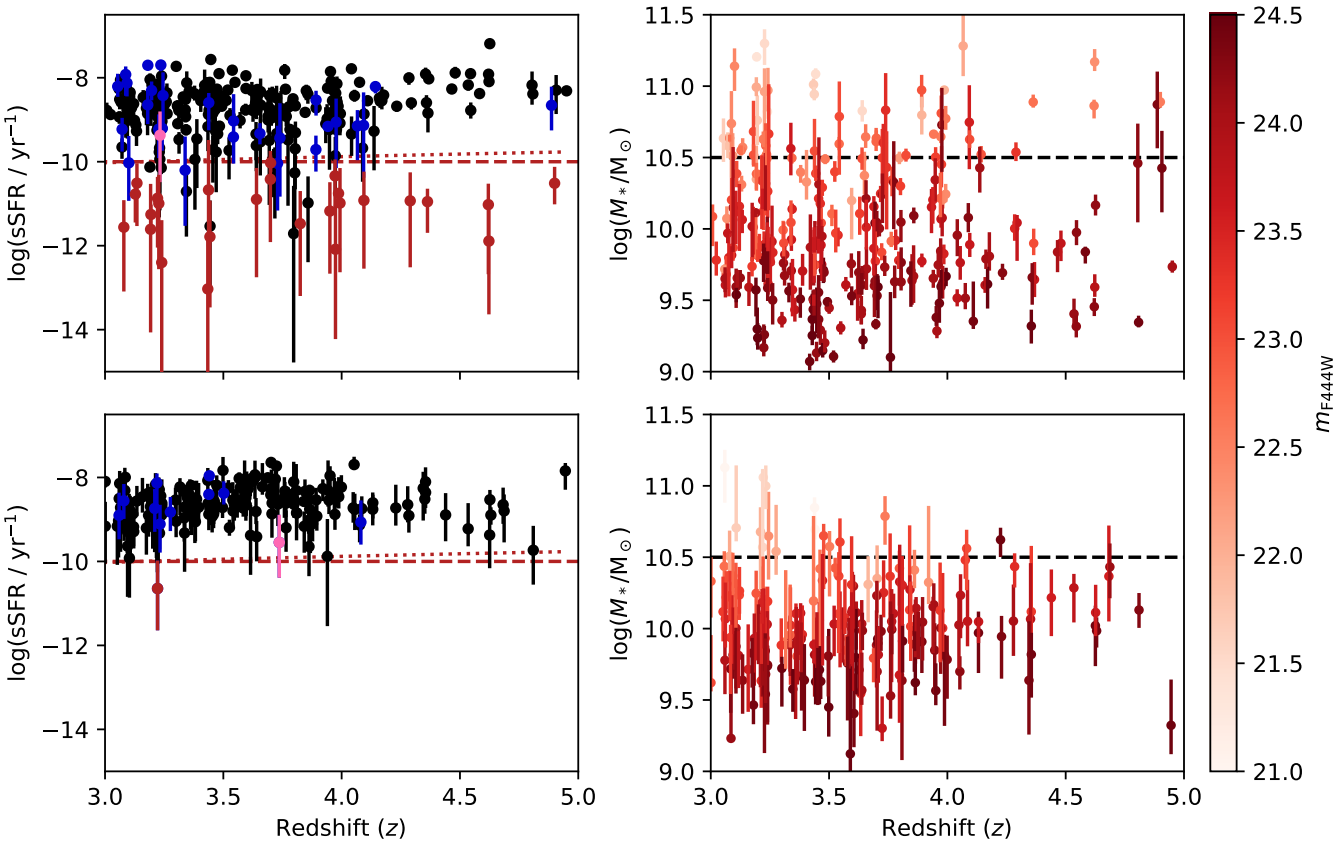


Figure 2. Top left: specific star formation rate versus redshift for spectroscopically confirmed galaxies modeled with `Prospector`. The dashed red line indicates the $\log(\mathrm{sSFR}/\mathrm{yr}^{-1}) < -10$ selection we use in this work, and the dotted red line shows the alternative $\mathrm{sSFR} < 0.2\ \mathrm{yr}^{-1}$ selection. Our results are robust to the choice in sSFR cut. The top histogram shows the nonnormalized distribution of redshifts of all galaxies (black), MSFGs (blue), and MQGs. The few pink points show massive marginally quiescent galaxies ($\log(\mathrm{sSFR}_{16}/\mathrm{yr}^{-1}) < -10$). Top right: stellar mass versus redshift for the same galaxies in the left panel, with points colored by F444W magnitude to demonstrate the mass-completeness limit selected. Bottom row: the same schematic as the top row, except for the set of galaxies for which only photometry was modeled at z_{spec}.

"marginally quiescent" (as in Y. Zhang et al. 2026a) and are shown in pink in Figures 1, 2, 3, and A1.

We also perform a cut in dust optical depth. After visually inspecting all spectra and models, we note that three galaxies with inferred $\log(M_*/M_\odot) \geqslant 10.5$ and $\log(\mathrm{sSFR}/\mathrm{yr}^{-1}) < -10$ have spectra and SEDs more consistent with dusty star-forming galaxies than quiescent galaxies. The uncertainties on $\log \mathrm{sSFR}/\mathrm{yr}^{-1} \approx 1$ dex, and the inferred SFHs all appear flat and relatively constant with high uncertainties, as might be expected for prior-dominated fits. Though there is evidence of high dust obscuration in quiescent galaxies (D. J. Setton et al. 2024; J. C. Siegel et al. 2025), out of an abundance of caution, we assume that all dusty galaxies ($\tau_{\mathrm{dust}} \geqslant 1.5$) are also star-forming. Three galaxies are rejected from the massive quiescent category, five are rejected from the massive marginally quiescent category, and five are rejected from the moderate-mass marginally quiescent category due to this selection. We show their NIRSpec spectra and best-fit `Prospector` models in Figure A2. Because only a few fits have both low sSFR and high dust optical depths, our results do not change if the $\tau_{\mathrm{dust}} < 1.5$ selection is not implemented for quiescent galaxies.

We show the spectra and maximum a posteriori SED models in Figure 1 for the 26 (1) NIRSpec spectra for sources classified as massive (marginally) quiescent galaxies (see also Table 1). The MQG SEDs all feature prominent Balmer/4000 Å breaks and low UV flux, indicative of evolved stellar populations and minimal ongoing star formation. We show $10 \leqslant \log(M_*/M_\odot) < 10.5$ quiescent and marginally quiescent galaxies in Figure A1 and Table A1. In these instances, galaxies classified as quiescent also show strong breaks and little UV flux, but the galaxies selected as "marginally quiescent" exhibit notably blue UV slopes, bright emission lines, and large uncertainties in sSFR (∼0.5–1 dex). We include the marginally quiescent moderate-mass galaxies in Figure A1 and Table A1 for completeness.

3.3. Photometric Prospector Modeling and MQG Selection

To obtain stellar population properties for the subset of 188 $3 < z_{\mathrm{spec}} < 5$, $m_{\mathrm{F444W}} < 24.5$ sources that have ground-based/HST spectroscopic redshifts or JWST spectra with low S/N or coverage in the rest-frame optical, we fit their photometry alone with Prospector, fixing redshifts to z_{spec}. Following the framework from B. Wang et al. (2024), we use the neural net emulator `parrot` (E. P. Mathews et al. 2023) which mimics FSPS models for faster photometric fits. The `parrot` emulator is trained on the fixed Prospector-α (J. Leja et al. 2017) and Prospector-β (B. Wang et al. 2023) models, so to ensure that our results are not strongly driven by the choice of photometric model, we ran both. We adopt the properties inferred with Prospector-α in this work, but note that our findings in Section 5 are invariant to the choice of either Prospector-α or Prospector-β in modeling photometry at fixed z_{spec}. These galaxies are included in the peak analysis in

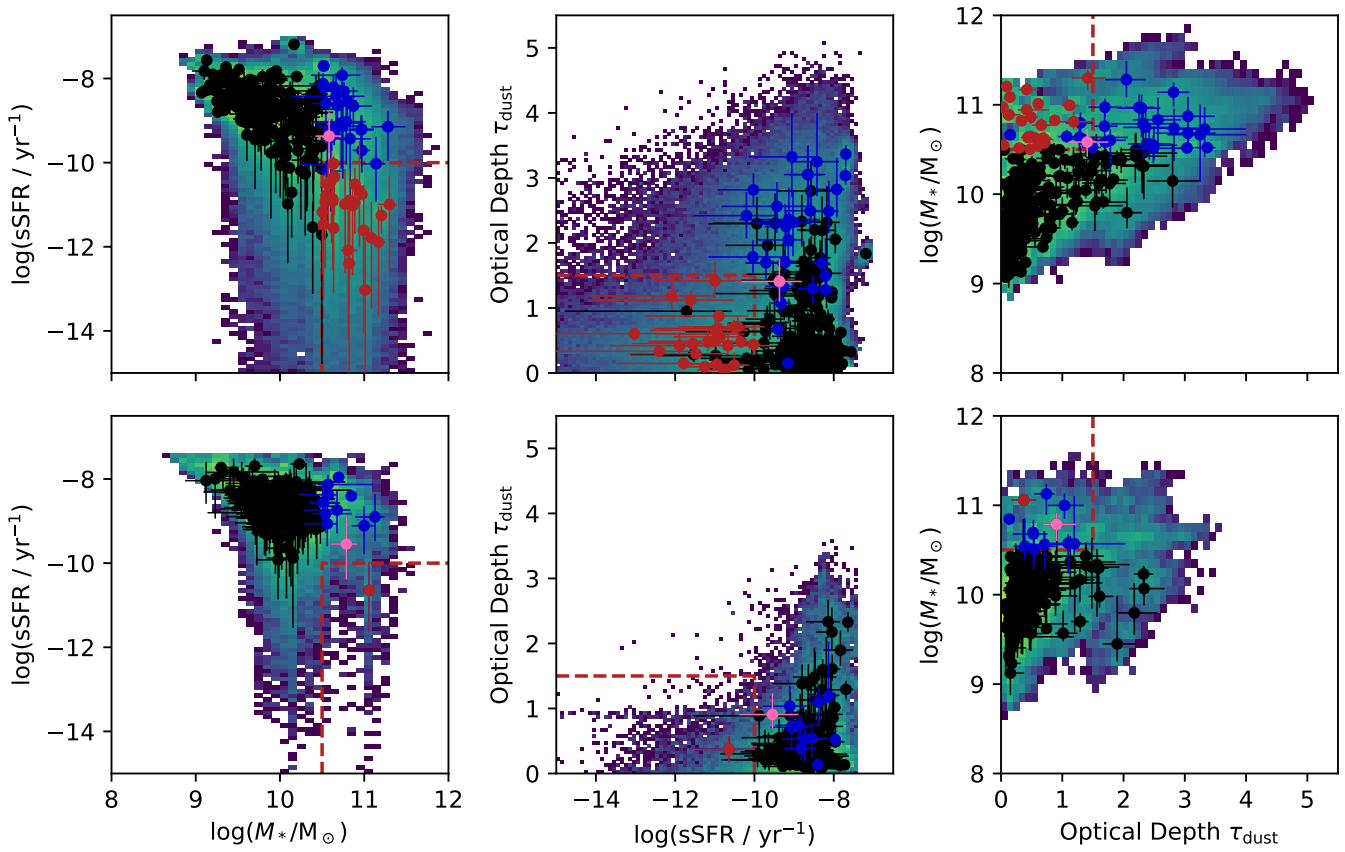


Figure 3. Top left: a two-dimensional histogram of $\log(M_*/M_\odot)$ and $\log(\mathrm{sSFR}/\mathrm{yr}^{-1})$ from the posterior draws of all $m_{\mathrm{F444W}} < 24$ spectroscopically confirmed galaxies modeled with `Prospector`. The individual galaxies and their uncertainties are indicated by black/blue/red/pink for galaxies classified as $\log(M_*/M_\odot) < 10.5/\log(M_*/M_\odot) \geqslant 10.5$ star-forming/$\log(M_*/M_\odot) \geqslant 10.5$ quiescent/$\log(M_*/M_\odot) \geqslant 10.5$ marginally quiescent based on their inferred posterior medians. The red box denotes the region we use to define MQGs. Top middle: same as the left, but for $\log(\mathrm{sSFR}/\mathrm{yr}^{-1})$ and optical depth τ_{dust}. Galaxies with high τ_{dust} and low sSFR appear to be dusty star-forming galaxies based on visual inspection of their spectra and SEDs. Top right: same as the left, but for $\log(M_*/M_\odot)$ and dust optical depth τ_{dust}. Bottom row: the same layout as the top row, except showing the inferred properties from galaxies with only fits to photometry at z_{spec} in Section 3.3.

Section 4, but we do not include them in Section 6 due to uncertainties in their SFHs. We show the inferred properties of these galaxies in the lower rows of Figures 2 and 3. The fits and imaging cutouts of the 16 photometrically modeled galaxies with $\log(M_*/M_\odot) \geqslant 10.5$ were visually inspected to check for contaminants in the MQG/MSFG samples. Fourteen are identified as star-forming galaxies, and we see no evidence in observed color (e.g., strong Balmer breaks and faint UV continuum slopes) or morphology (e.g., Little Red Dot–like) to suggest otherwise.

One photometrically modeled galaxy fits our MQG criteria and has observed colors consistent with a large Balmer break. The redshift for ID 62676 at R.A. = 34.274154, decl. = −5.227383, and $z = 3.222$ is included as a ground-based redshift in the 3D-HST catalog. We queried the DJA MOSFIRE extractions and found that ID 62676 was observed in the K band (U069M, PI: Illingworth; W182M, PI: Glazebrook). From visual inspection of the two-dimensional spectrum, we easily identified the [O III] emission doublet at ∼2.1 μm and tentative Hβ absorption at ∼2.06 μm in the clearly visible stellar continuum.

Another is classified as marginally quiescent with a photometric break: RUBIES-19785, at $z = 3.73$, has a RUBIES G395M spectrum in which Hα and [N II] emission are visible, though the spectrum only extends to ∼6000 Å rest frame. From the precomputed DJA emission-line catalogs, we calculate [N II]/Hα = 0.96 ± 0.07, which is suggestive of AGN activity.

4. Quantifying Environment

In the era of JWST, both the number and maximum redshift of protostructures and protostructure candidates have increased dramatically. Many of these were discovered by looking for overdensities using redshifts from photometry (R. Pan et al. 2025), slit spectroscopy (T. Morishita et al. 2023; A. C. Carnall et al. 2024; A. de Graaff et al. 2025a; L. Napolitano et al. 2025), slitless spectroscopy (J. M. Helton et al. 2024a; J. B. Champagne et al. 2025a, 2025b; Y. Fudamoto et al. 2026; X. Lin et al. 2026), or some combination thereof (N. Laporte et al. 2022; J. M. Helton et al. 2024b; S. Jin et al. 2024; S. M. Urbano Stawinski et al. 2024a).

4.1. Overdensity Maps

To recover the underlying cosmic density field, we employ a Voronoi tessellation method, applied to both spectroscopy and photometry. B. Darvish et al. (2015) first introduced the "weighted Voronoi tessellation estimator" among a collection of other density estimator methods. Of all methods presented, it was shown that the Voronoi method and the weighted adaptive kernel method best recovered the true underlying density. While weighted kernel density estimators have been

Table 1
Massive Quiescent Galaxies

ID	R.A. (deg)	Decl. (deg)	$z_{\rm spec}$	$\log(M_*/M_\odot)$	$\rm SFR_{10Myr}$ ($M_\odot$ yr^{-1})	$\log(\delta_{\rm gal}+1)$	Programs
DeepDive-38239[b]	34.427658	−5.152416	3.228	$11.30^{+0.09}_{-0.14}$	$1.9^{+7.2}_{-1.9}$	$0.25^{+0.14}_{-0.18}$	5
ZF-UDS-7329	34.255875	−5.233825	3.194	$11.20^{+0.02}_{-0.02}$	$0.9^{+0.6}_{-0.6}$	$0.63^{+0.18}_{-0.17}$	3, 4
EXCELS-117560	34.399660	−5.136357	4.619	$11.17^{+0.08}_{-0.05}$	$0.2^{+1.2}_{-0.2}$	$0.47^{+0.30}_{-0.29}$	4, 5, 7
DeepDive-61167	214.866042	52.884089	3.444	$11.09^{+0.03}_{-0.02}$	$0.2^{+1.3}_{-0.2}$	$1.20^{+0.00}_{-0.00}$	5
2565-31322	214.866054	52.884256	3.436	$11.01^{+0.03}_{-0.03}$	$0.0^{+0.2}_{-0.0}$	$0.65^{+0.17}_{-0.11}$	3, 5, 7
EXCELS-57000	34.258890	−5.232293	3.193	$10.99^{+0.06}_{-0.05}$	$0.2^{+2.5}_{-0.2}$	$0.37^{+0.36}_{-0.22}$	3, 4, 7
EXCELS-50789	34.340363	−5.241275	3.987	$10.97^{+0.02}_{-0.01}$	$1.7^{+0.5}_{-0.5}$	$0.96^{+0.05}_{-0.72}$	3, 4
CEERS-2759	214.871231	52.845066	3.439	$10.94^{+0.04}_{-0.03}$	$1.9^{+27.5}_{-1.8}$	$0.21^{+0.28}_{-0.15}$	2, 7
RUBIES-EGS-QG-1	214.915546	52.949018	4.896	$10.89^{+0.06}_{-0.03}$	$2.4^{+4.0}_{-1.6}$	$0.62^{+0.20}_{-0.19}$	7
EXCELS-65915	34.280543	−5.217151	4.359	$10.89^{+0.04}_{-0.03}$	$0.9^{+0.9}_{-0.7}$	$0.79^{+0.41}_{-0.27}$	4, 7
EXCELS-109760	34.365072	−5.148846	4.621	$10.86^{+0.03}_{-0.08}$	$0.7^{+1.5}_{-0.7}$	$0.51^{+0.16}_{-0.12}$	4, 7
RUBIES-55077[b]	214.853899	52.861365	3.641	$10.83^{+0.06}_{-0.06}$	$0.9^{+3.6}_{-0.8}$	$0.60^{+0.39}_{-0.19}$	3, 7
DeepDive-40442	214.895613	52.856498	3.239	$10.82^{+0.04}_{-0.04}$	$0.0^{+0.2}_{-0.0}$	$0.38^{+0.12}_{-0.11}$	2, 3, 5
MoM-137836	34.360159	−5.153092	3.982	$10.81^{+0.11}_{-0.09}$	$0.1^{+0.6}_{-0.1}$	$1.36^{+0.20}_{-0.00}$	4, 7, 8
RUBIES-12594	34.368535	−5.299475	3.994	$10.77^{+0.08}_{-0.07}$	$0.6^{+3.2}_{-0.6}$	$0.47^{+0.18}_{-0.15}$	7
MoM-144670	34.242593	−5.143121	3.974	$10.65^{+0.03}_{-0.03}$	$2.0^{+3.0}_{-1.8}$	$0.09^{+0.22}_{-0.19}$	4, 8
EXCELS-45981	34.364641	−5.250241	3.079	$10.64^{+0.01}_{-0.01}$	$0.1^{+0.4}_{-0.1}$	$0.34^{+0.25}_{-0.18}$	4
EXCELS-39063	34.290443	−5.262081	3.701	$10.64^{+0.04}_{-0.04}$	$4.1^{+2.0}_{-1.6}$	$0.24^{+0.33}_{-0.21}$	3, 4
4106-76085	214.836844	52.873457	3.221	$10.63^{+0.04}_{-0.04}$	$0.6^{+1.3}_{-0.5}$	$0.12^{+0.31}_{-0.23}$	6
RUBIES-155916	34.317031	−5.127611	4.098	$10.63^{+0.05}_{-0.05}$	$0.5^{+1.9}_{-0.5}$	$0.23^{+0.23}_{-0.21}$	7
RUBIES-18302	34.233628	−5.283850	3.703	$10.61^{+0.08}_{-0.05}$	$1.6^{+5.3}_{-1.5}$	$0.39^{+0.29}_{-0.22}$	7
RUBIES-61712[*]	34.240916	−5.205573	3.236	$10.58^{+0.15}_{-0.16}$	$16.3^{+29.0}_{-14.7}$	$0.17^{+0.18}_{-0.22}$	7
RUBIES-175698	34.227642	−5.099286	3.142	$10.57^{+0.05}_{-0.03}$	$1.2^{+2.2}_{-1.0}$	$0.16^{+0.27}_{-0.24}$	7
CAPERS-16184	34.513656	−5.157829	3.123	$10.55^{+0.02}_{-0.02}$	$0.6^{+0.6}_{-0.5}$	$0.23^{+0.32}_{-0.24}$	9
WIDE-4358	215.039079	53.002774	4.283	$10.54^{+0.06}_{-0.05}$	$0.4^{+1.5}_{-0.4}$	$0.22^{+0.23}_{-0.33}$	1
RUBIES-180345	34.209839	−5.091602	3.830	$10.52^{+0.03}_{-0.03}$	$0.1^{+0.6}_{-0.1}$	$-0.01^{+0.14}_{-0.17}$	7
WIDE-3330	34.338199	−5.166202	3.937	$10.50^{+0.06}_{-0.05}$	$0.2^{+0.8}_{-0.2}$	$0.17^{+0.25}_{-0.20}$	1
ID-62676[b]	34.274154	−5.227383	3.222	$11.06^{+0.05}_{-0.06}$	$2.6^{+9.0}_{-2.3}$	$0.65^{+0.25}_{-0.22}$	⋯
RUBIES-19785[a]	34.330968	−5.287484	3.736	$10.79^{+0.13}_{-0.19}$	$18.3^{+40.5}_{-15.6}$	$0.64^{+0.18}_{-0.17}$	7

Notes. Massive quiescent and marginally quiescent galaxies ordered by $\log(M_*/M_\odot)$. Survey identifiers are assigned based on the spectrum used for SED modeling. For the prominent MQGs featured in K. Glazebrook et al. (2024) and A. de Graaff et al. (2025a), we use the names given in those works. Otherwise, MQG IDs are given as [survey]-[field]-[source ID] or [program ID]-[field]-[source ID] if a survey name is not available. In the "Programs" column, we list the JWST programs that obtained spectra of each galaxy, ordered numerically by program ID: (1) 1213/1215, WIDE (M. V. Maseda et al. 2024); (2) 1345, CEERS (S. L. Finkelstein et al. 2023); (3) 2565 (T. Nanayakkara et al. 2024; T. Nanayakkara et al. 2025); (4) 3543, EXCELS (A. C. Carnall et al. 2024; H. H. Leung et al. 2026); (5) 3567, DeepDive (M. L. Hamadouche et al. 2026; K. Ito et al. 2026); (6) 4106 (PI: E. Nelson); (7) 4233, RUBIES (A. de Graaff et al. 2025b; Y. Zhang et al. 2026a); (8) 5224, Mirage or Miracle (PI: P. Oesch); (9) 6368, CAPERS (PI: M. Dickinson). The properties of the two entries at the bottom of the table (ID-62676 and RUBIES-19785) were inferred from modeling their photometry alone.

[a] Marginally quiescent with $\log(\rm sSFR_{16}/yr^{-1}) < -10$, not included in Sections 6.2 and 6.3.

[b] Uncertain SFH due to lack of spectral coverage in the break, not included in Sections 6.2 and 6.3.

used to measure environments in other studies (N. Chartab et al. 2020; I. McConachie et al. 2022; S. M. Urbano Stawinski et al. 2024a; I. McConachie et al. 2025), they are sensitive to the size and form of the kernel and are typically spatially symmetric, which can be disadvantageous when trying to recover the shapes of often asymmetric and "lumpy" protostructures (e.g., S. I. Muldrew et al. 2015; R.-S. Remus et al. 2023). Conversely, a Voronoi tessellation requires no size calibration and assumes no underlying geometry. The framework for our Voronoi tessellation method was based on and most closely resembles the "Voronoi Monte Carlo" (VMC) method first presented in B. C. Lemaux et al. (2018), which has been subsequently utilized in, e.g., A. R. Tomczak et al. (2017), O. Cucciati et al. (2018), D. Hung et al. (2020), L. Shen et al. (2021), B. C. Lemaux et al. (2022), B. Forrest et al. (2023), E. A. Shah et al. (2024), and D. Hung et al. (2025). We provide a brief summary in the following paragraph; those interested in the specifics can find a detailed version in Appendix B.

First, we produce Cartesian grids of the UDS and EGS fields in a transformed coordinate plane such that the fields are equatorial (R.A.′ and decl.′; the EGS is also rotated by 49 degrees counterclockwise in the prime frame). We resample redshifts from a spectroscopic $p(z)$ when $z_{\rm spec}$ is available or the photometric $p(z)$ otherwise. For a given target redshift, we retain galaxies with redshifts lying within a narrow slice with a line-of-sight width equal to 10 cMpc and centered on the target redshift. We partition the field grid using a Voronoi tessellation. The pixels in each cell are assigned values equal to the inverse of the entire cell's area (i.e., the cell's galaxy surface density $\Sigma_{\rm gal}$). We perform 100 iterations and take the median, 16th, and 84th percentile values of each pixel to be the

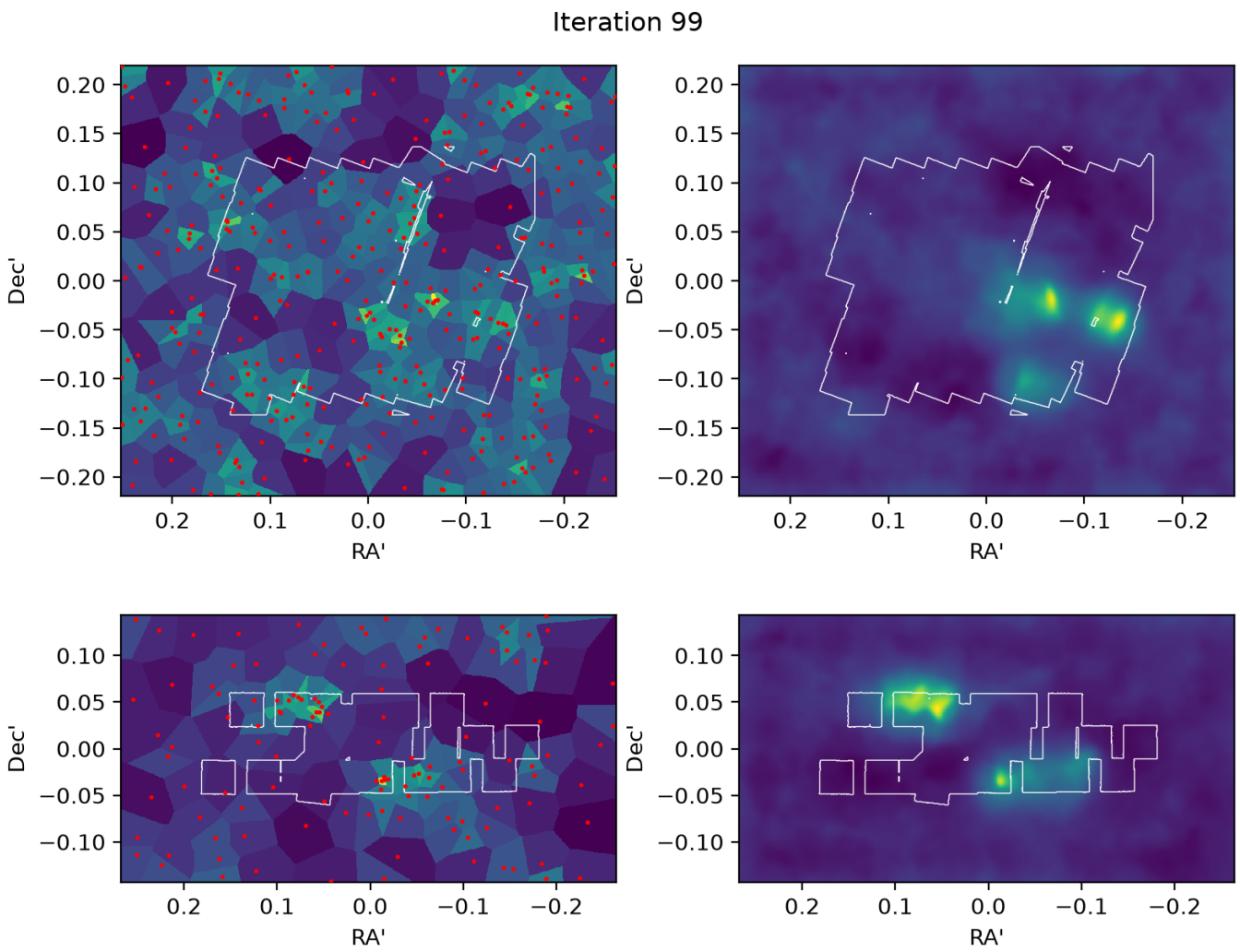


Figure 4. The MCVT process at $z = 3.193$ in the UDS (top) and $z = 4.891$ in the EGS (bottom). The left panels show the final single iteration of the MCVT process. Red points are the coordinates of galaxies that fall into the redshift slice in the given iteration. Each cell is colored according to the inverse of its area. Panels on the right show the stacked medians of all 100 iterations, smoothed by a Gaussian filter with a width of 2.5 pixels. In both panels the white contour shows the outline for the F444W footprints and the color density scaling is left arbitrary. The fields are shown in the R.A.′ and decl.′ coordinate frame. An animated version showing the construction of the median image for all 100 iterations is available in the online journal. The real-time duration of the animation is 15 s.

(An animation of this figure is available in the online article.)

density and its associated lower and upper uncertainties. Galaxy surface densities are converted into galaxy overdensities $\delta_{\rm gal} = \Sigma_{\rm gal}/\overline{\Sigma}_{\rm gal} - 1$.

We refer to this method as Monte Carlo Voronoi tessellation (MCVT), which is similar to VMC mapping (e.g., B. C. Lemaux et al. 2018) but distinct in setup and execution. In Figure 4, we show a single iteration on the left and the stacked median on the right (in the online journal, an animation shows all iterations and the development of the median image). Red points denote the location of the redshift slice members for a given iteration, and the field grid pixels are colored (with arbitrary scaling) by their $\log \Sigma_{\rm gal}$. White contours indicate the boundaries of the F444W footprint. With successive iterations, structures that are not detectable in individual iteration maps begin to appear in the median image.

With the ability to produce galaxy overdensity maps of the UDS and EGS fields at any redshift $z_{\rm slice}$, we then walk through redshift space from $3 \leqslant z_{\rm slice} \leqslant 5$ in 1 cMpc steps, performing the MCVT at each redshift step. Indexing $z_{\rm slice}$ by k, for each field we construct a three-dimensional density grid of voxels with values $\delta_{\rm gal}^{i,j,k}$, where i, j, and k are tied to locations in R.A.′, decl.′, and redshift-z space, respectively. We show cross sections of the density grids in Figure 5, with the top pair showing the UDS and the bottom pair showing the EGS. Of each pair, the upper plot shows overdensity in R.A.′ and redshift maximized over decl.′, and the lower shows overdensity in decl.′ and redshift maximized over R.A.′ (i.e., $\delta_{\rm gal}^{i,k}$ and $\delta_{\rm gal}^{j,k}$, respectively). The locations of MQGs are shown by large red stars, and massive marginally quiescent galaxies by pink large stars. Galaxies with $10 \leqslant \log(M_*/M_\odot) < 10.5$ classified as quiescent or marginally quiescent are shown by smaller stars with the same coloring scheme. Remarkably, the MQG population appears to coincide strongly with regions of high overdensity in the galaxy maps. We explore this trend in greater detail in Section 5.

4.2. Structure Identification

With our three-dimensional R.A.–decl.–z density grids in hand, we next identify prominent density peaks and

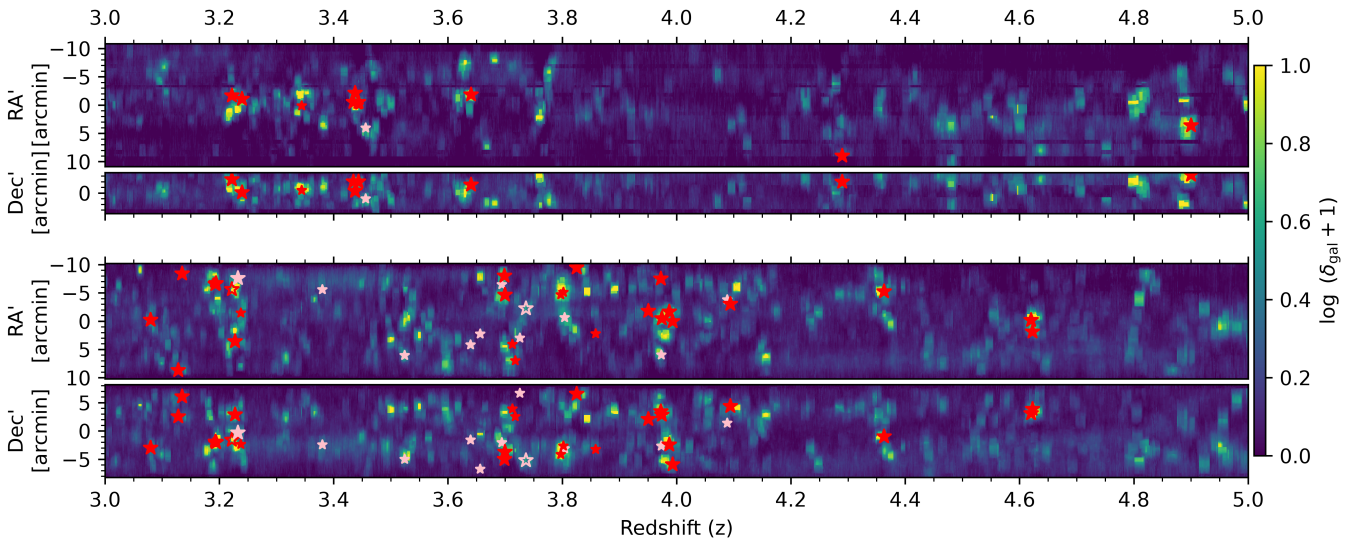


Figure 5. Cross sections of the $3 < z < 5$ density grids in the EGS (top) and UDS (bottom) fields with redshift along the x-axis and decl.′ and R.A.′ on the y-axes. The locations of the quiescent galaxies from Section 3 are indicated by larger red stars, and marginally quiescent galaxies by pink stars. Open stars correspond to the photometry-only fits in Section 3.3. Smaller red (pink) stars show the positions of $10 \leqslant \log(M_*/M_\odot) < 10.5$ (marginally) quiescent galaxies. Several previously identified overdensities are immediately recognizable: in UDS, the $z = 3.2$ overdensity in UDS around ZF-UDS-7329 (C. K. Jespersen et al. 2025; C. Turner et al. 2025; L. Kawinwanichakij et al. 2026), the $z = 4.6$ overdensity around EXCELS-117560 and EXCELS-109760 (A. C. Carnall et al. 2024; C. K. Jespersen et al. 2025); in EGS, the Cosmic Vine at $z = 3.4$ (S. Jin et al. 2024; K. Ito et al. 2025; N. B. Sillassen et al. 2026) and the overdensity around the $z = 4.9$ quiescent galaxy RUBIES-EGS-QG1 (S. M. Urbano Stawinski et al. 2024a; A. de Graaff et al. 2025a). Remarkably, almost all spectroscopically confirmed quiescent galaxies seem to be found in or near an overdensity.

surrounding overdense structures. First, we confirm that median $\log(\delta_{\rm gal} + 1) = 0$, and iteratively fit a 3σ-clipped Gaussian centered at zero to $\log(\delta_{\rm gal} + 1)$. We take the dispersion of this Gaussian to be $\sigma_{\log(\delta_{\rm gal}+1)}$.

4.2.1. Overdense Peaks

To identify overdense peaks, we isolate all voxels with $\log(\delta_{\rm gal} + 1) > 5\sigma_{\log(\delta_{\rm gal}+1)}$ (hereafter "peak voxels"). We use the clustering algorithm DBSCAN in the `scikit-learn` python package to produce groups of contiguous peak voxels. Each group is flagged as an individual overdense peak. For each peak, we convert the galaxy overdensity to a matter density, which we integrate over the volume of the peak to estimate a peak mass:

$$M_{\rm peak} = \sum_{i,j,k}^{\rm Peak} M_{i,j,k} = \sum_{i,j,k}^{\rm Peak} V_{i,j,k}\rho_m(1 + \frac{\delta_{gal}^{i,j,k}}{b(z_k)}), \quad (1)$$

where $V_{i,j,k}$ is the comoving volume of each peak voxel with index i, j, and k (because each z-slice is 10 cMpc thick and we take 1 cMpc steps in z, we set the line-of-sight depth of every voxel to be 1 cMpc), ρ_m is the comoving matter density of the Universe, and $b(z_k)$ is the redshift-dependent galaxy bias parameter, which relates galaxy density to the underlying matter density distribution $b = \delta_{\rm gal}/\delta_{\rm m}$ taken from R. L. Barone-Nugent et al. (2014) and derived based on the clustering of Lyman-break galaxies observed with HST. The majority of sources in our $3 < z < 5$ spectroscopic catalog are blue and star-forming, but to confirm that this choice does not strongly bias our results, we produced a second set of density maps restricted to those with UV-bright best-fit `eazy` models at their resampled redshifts. We find generally good agreement, with ∼0.1 dex scatter between $M_{\rm peak}$ calculated from matching volumes in the two sets of maps.

We rank the robustness of peaks by their mass and galaxy membership. We consider peaks with $10^{12} \leqslant M_{\rm peak} < 10^{13} M_\odot$ to be low-confidence overdensity detections (hereafter minor peaks or subpeaks). Upon visual inspection, these minor peaks often correspond to low overdensity over a large volume or moderate overdensity in a small volume with $\lesssim$3 spectroscopic members, are often located near field edges where density measurements are closer to the median and highly uncertain, and rarely host massive galaxies. Peaks with $M_{\rm peak} \geqslant 10^{13} M_\odot$ are taken to be moderate-confidence overdensity detections and represent regions with high galaxy density over a large volume. For a peak to be considered a high-confidence overdensity detection (hereafter a "robust overdensity"), we require $M_{\rm peak} \geqslant 10^{13} M_\odot$ and the peak to contain at least one $\log(M_*/M_\odot) \geqslant 10.5$ galaxy or three $\log(M_*/M_\odot) \geqslant 10$ galaxies, as an indication that the galaxy number overdensity also traces a large mass. In future works, we will calibrate this peak-selection method in comparisons with simulations and explore how $M_{\rm peak}$ relates to $M_{\rm halo}$.

For each moderate and robust peak, we calculate a barycenter position (as in, e.g., O. Cucciati et al. 2018; L. Shen et al. 2021; B. Forrest et al. 2023; E. A. Shah et al. 2024). We convert each voxel's coordinates R.A.$_i'$, decl.$_j'$, z_k into comoving coordinates X_i, Y_j, Z_k. For each comoving coordinate C and associated index m, the barycenter comoving coordinate is given by $C_{\rm bary} = \sum_m (C_m \delta^m_{\rm gal})/\sum_m \delta^m_{\rm gal}$ (i.e., the overdensity-weighted average of comoving coordinate C). Robust peaks are assigned identifiers [field]-Peak-z[redshift], and moderate-density peaks are assigned [field]-cPeak-z[redshift], where cPeak indicates that these are candidate overdensities that will require further analysis for confirmation. We give peak IDs, barycenter locations in R.A., decl., and redshift, peak mass and volume, and the numbers of high-mass ($M_* \geqslant 10^{10.5} M_\odot$), moderate-mass ($10^{10} M_\odot \leqslant M_* < 10^{10.5} M_\odot$), and NIRSpec-confirmed members in Table 2 for robust peaks. The same

Table 2
Robust Overdensity Peaks

ID	$z_{\rm Bary}$	R.A.$_{\rm Bary}$ (deg)	Decl.$_{\rm Bary}$ (deg)	$\log(M_{\rm Peak}/M_\odot)$	Volume (cMpc^3)	$N_{\rm HM}$[a]	$N_{\rm MM}$[b]	$N_{\rm spec}$[c]
UDS-Peak-z3.2-1	3.187	34.255885	−5.248896	13.3	282	3	5	11
UDS-Peak-z3.2-2	3.228	34.267417	−5.239503	13.6	503	2	1	17
UDS-Peak-z3.2-3	3.240	34.349323	−5.262120	13.3	331	1	4	8
UDS-Peak-z3.6	3.598	34.484781	−5.145062	13.5	467	0	4	8
UDS-Peak-z3.7-1	3.694	34.267736	−5.239406	13.7	665	1	1	18
UDS-Peak-z3.7-2	3.732	34.356205	−5.281517	13.0	177	1	1	6
UDS-Peak-z3.8	3.801	34.289935	−5.261519	14.1	1510	0	6	27
UDS-Peak-z3.9	3.891	34.272921	−5.141617	13.0	131	1	1	5
UDS-Peak-z4.0-1	3.978	34.354284	−5.179573	13.8	978	2	2	23
UDS-Peak-z4.0-2	3.984	34.397822	−5.293444	13.4	354	1	3	11
UDS-Peak-z4.1	4.103	34.271445	−5.135420	13.0	153	1	0	5
UDS-Peak-z4.6	4.623	34.369135	−5.143463	13.6	504	2	1	13
EGS-Peak-z3.2	3.227	214.905853	52.884083	13.7	712	3	3	33
The Leaf[d]	3.346	214.868027	52.848001	13.6	524	1	0	18
EGS-Peak-z3.4-1	3.441	214.874314	52.884051	13.4	301	3	2	29
EGS-Peak-z3.4-2	3.464	215.027895	52.910927	13.3	272	1	3	9
EGS-Peak-z3.6	3.629	214.880393	52.863926	13.4	337	1	2	13
EGS-Peak-z4.9-1	4.887	214.912448	52.820067	13.4	339	1	0	7
EGS-Peak-z4.9-2	4.894	214.931566	52.950079	13.6	574	1	0	13

Notes. We include a table of candidate overdensities (i.e., moderate-confidence overdensity peaks) in Appendix C.
[a] The number of high-mass galaxies with $\log(M_*/M_\odot) \geqslant 10.5$ in the overdense peak.
[b] The number of moderate-mass galaxies with $10 \leqslant \log(M_*/M_\odot) < 10.5$ in the overdense peak.
[c] The number of spectroscopically confirmed galaxies in the overdense peak.
[d] N. B. Sillassen et al. (2026).

Table 3
Protoclusters

ID	$z_{\rm Bary}$	R.A.$_{\rm Bary}$ (deg)	Decl.$_{\rm Bary}$ (deg)	$\log(M_{\rm Struct}/M_\odot)$	Volume (cMpc^3)	$N_{\rm HM}$[a]	$N_{\rm MM}$[b]	$N_{\rm spec}$[c]
UDS-PCl-z3.2	3.217	34.319954	−5.225294	14.46	4820	8	14	78
UDS-PCl-z3.7	3.693	34.272547	−5.239969	13.96	1507	2	1	20
UDS-PCl-z3.8	3.803	34.291929	−5.261763	14.35	3647	0	6	31
UDS-PCl-z4.0	3.980	34.371199	−5.207072	14.35	3752	3	7	53
EGS-PCl-z3.2	3.228	214.903756	52.881273	14.01	1626	3	5	44
Cosmic Vine-1[d]	3.440	214.875224	52.882571	13.59	515	4	2	33
Cosmic Vine-2[d]	3.459	215.011252	52.895611	13.70	883	1	3	21
EGS-PCl-z4.9	4.889	214.932621	52.948949	13.90	1310	1	0	14

Notes.
[a] The number of high-mass galaxies with $\log(M_*/M_\odot) \geqslant 10.5$ in the protocluster.
[b] The number of moderate-mass galaxies with $10 \leqslant \log(M_*/M_\odot) < 10.5$ in the protocluster.
[c] The number of spectroscopically confirmed galaxies in the protocluster.
[d] In our density maps the Cosmic Vine (S. Jin et al. 2024; N. B. Sillassen et al. 2026) is fragmented into two halves separated by ∼100 pkpc (see Figure 6).

quantities for moderate-confidence peaks (i.e., candidate overdensities) are given in Appendix C, minus the number of high-mass spectroscopically confirmed members.

4.2.2. Protocluster Identification

Simulations show that the galaxies which are found in $z = 0$ clusters and other cosmic structures are found spread across tens of comoving megaparsecs in the high-redshift universe (Y.-K. Chiang et al. 2013; S. I. Muldrew et al. 2015; R.-S. Remus et al. 2023). To identify potential extended large-scale structure around the overdense peaks in Section 4.2.1, we lower the density threshold to $3\sigma_{\log(\delta_{\rm gal}+1)}$, taking all voxels above this threshold to be "structure voxels." As we did for the peaks, we identify contiguous groups of structure voxels and calculate masses and barycenters of structures. Structures containing a robust peak detection and with estimated mass in excess of that of the Fornax Cluster ($M_{\rm struct} > 10^{13.85}$; M. J. Drinkwater et al. 2001) are labeled "protoclusters." Identifiers for new protoclusters are assigned as [field]-PCl-z[redshift]; otherwise, the name from the literature is given. We show the properties of these protoclusters in Table 3 and a three-dimensional plot of UDS-PCl-z3.2 in Figure 6 (an interactive version with all protoclusters is available in the online journal).

UDS-PCl-z3.2. Previous studies identified an overdensity around the quiescent galaxy ZF-UDS-7329 (K. Glazebrook et al. 2024; C. K. Jespersen et al. 2025; C. Turner et al. 2025). In our density mapping, we identify several overdense peaks (three robust detections and one moderate-confidence detection; Tables 2 and C1) contained within an extended protocluster. ZF-UDS-7329 lies just within the 5σ contour of

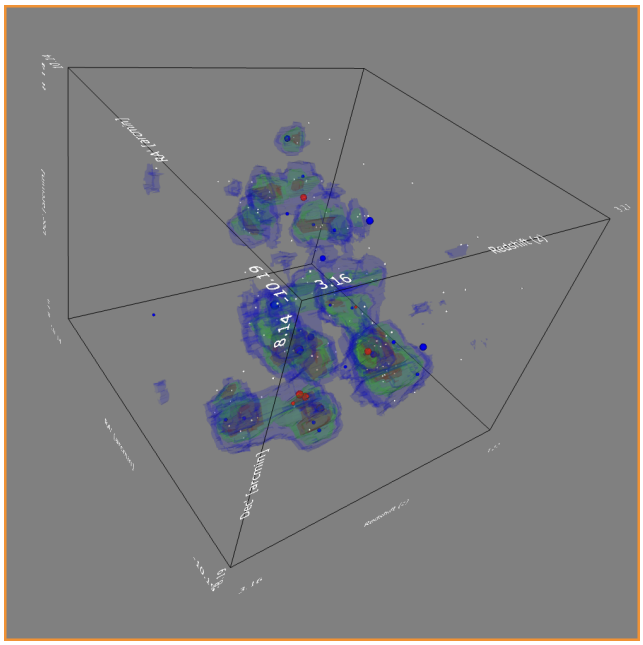


Figure 6. An isometric view of UDS-PCl-z3.2 from the MCVT mapping. We show $3\sigma/5\sigma/8\sigma$ contours as blue/green/red surfaces. Galaxies with $\log(M_*/M_\odot) \geqslant 10.5$ are shown as large colored spheres (red for quiescent, blue for star-forming), $10 \leqslant \log(M_*/M_\odot) < 10.5$ as smaller colored spheres, and all other spectroscopically confirmed galaxies as small white spheres. An interactive version of this figure is available in the online journal via the X3D-pathway (F. P. A. Vogt et al. 2016) for exploration (click and drag to rotate, scroll to zoom). In the interactive version, all protoclusters in Table 3 plus UDS-Peak-z4.6 are viewable via a dropdown menu and quiescent galaxies are labeled according to their IDs in Tables 1 and A1. Buttons are provided to align the viewer along the R.A.′ decl.′ z axes and to toggle the contours and quiescent galaxy labels on or off.

An interactive version of this figure is available in the online article.

UDS-Peak-z3.2-1, adjacent to the MQG EXCELS-57000 and the moderate-mass quiescent galaxy WIDE-5935.

UDS-PCl-z3.7 and UDS-PCl-z3.8. These two newly discovered protoclusters lie in the UDS, the first containing a MQG, the second several moderate-mass quiescent galaxies. Their ∼75 cMpc separation along the line of sight, while significant, is not unheard of for massive and extended high-redshift structures (e.g., O. Cucciati et al. 2018). In Figure 5 and the interactive version of Figure 6, there is a hint of a lower-density intervening filamentary structure between them at $z \sim 3.75$, containing UDS-Peak-z3.7-2. If this intervening structure is real, UDS-PCl-z3.7 and UDS-PCl-z3.8 could be part of a single large-scale protosupercluster, and are therefore prime candidates for further spectroscopic followup.

UDS-PCl-z4.0. M. Tanaka et al. (2024) first identified this structure as an overdensity of VANDELS spectroscopic redshifts at $z = 4$. Two additional $z = 4$ overdensities of quiescent galaxies lie just south (M. Tanaka et al. 2024) and north (T. Kakimoto et al. 2026a) of the PRIMER UDS footprint, indicating that this structure extends well beyond the volume observed here. We identify five $\log(M_*/M_\odot) \geqslant 10.5$ and one $10.0 \leqslant \log(M_*/M_\odot) < 10.5$ quiescent galaxies in and around this structure. This structure was independently identified by H. Sun et al. (2025) as "the Bigfoot". We note that for three of four peaks identified in this structure, we find that the UV-bright galaxy density maps infer noticeably lower $M_{\rm peak}$ with lower overall $\delta_{\rm gal}$. This could suggest that not all early cosmic structures host UV-bright galaxies (e.g., A. B. Newman et al. 2022, 2025).

EGS-PCl-z3.2. We find five massive galaxies (two of which are quiescent) in and around EGS-PCl-z3.2, a newly discovered protocluster. Unlike most other $3 < z < 4$ protoclusters in this work, which are typically spread out with many subpeaks within and nearby the structures, EGS-PCl-z3.2 appears relatively compact, with only a few minor foreground and background subpeaks. This could be an indication that this structure may be more evolved than the others presented here and undergoing gravitational collapse, or there may be extended overdense structure outside of the relatively small EGS footprint.

The Cosmic Vine. First identified in S. Jin et al. (2024), the $z = 3.44$ Cosmic Vine extends across the EGS field. The Cosmic Vine is also notable for hosting a high fraction of quiescent galaxies (N. B. Sillassen et al. 2026), with a pair merging in its core (IDs 2565-31322 and DeepDive-61167; K. Ito et al. 2025). 2565-31322 was presented in T. Nanayakkara et al. (2024) and featured heavily in the discussion relating morphology and environment in L. Kawinwanichakij et al. (2026). Another galaxy with a prominent Balmer break in its spectrum, WIDE-3098, at $z = 3.4407$, lies outside the EGS footprint (and is therefore not included in this work's analyses) to the northeast on the sky, due east in the R.A.′ decl.′ frame, between the "tongs." This could suggest that the Cosmic Vine structure extends outside of the EGS footprint and is larger than the extent inferred in this work or S. Jin et al. (2024) and N. B. Sillassen et al. (2026). In our density maps, the Cosmic Vine is fragmented into two components, the borders of which are separated by <100 pkpc. No other structures have such a small separation, so we include both components in Table 3 as their combined mass exceeds the minimum for consideration.

EGS-PCl-z4.9. EGS-PCl-z4.9 was identified as an overdensity in A. de Graaff et al. (2025a) and a protocluster in S. M. Urbano Stawinski et al. (2024a), though due to its location on the edge of the EGS, we lack the coverage to determine its extent beyond the field. Within the bounds of the EGS, we estimate the mass contained within the 3σ contour to be $\log(M_{\rm Struct}/M_\odot) = 13.90$, just barely above the protocluster classification cutoff. A small clump of star-forming galaxies originally identified in A. de Graaff et al. (2025a), EGS-Peak-z4.9-1, lies just south of EGS-Peak-z4.9 along the southern side of the field. We do not see any indication of intervening structure connecting these two overdensities.

UDS-Peak-z4.6. While not detected as a protocluster, this peak is notable in that it contains two of the highest-redshift MQGs yet discovered, EXCELS-117560 and EXCELS-109760 (A. C. Carnall et al. 2024). Whereas EGS-Peak-z4.9 lies within a protocluster and may extend outside of the EGS field, UDS-Peak-z4.6 is fairly isolated near the middle of the UDS field with no other indication of extended structure nearby. Though we find the $z > 4.5$ MQGs are all found in locally overdense environments, this peak demonstrates that the presence of a massive and extended protocluster is evidently not a strict prerequisite to forming MQGs.

5. Results

5.1. The Effects of Environment on $3 < z < 5$ Massive Quiescent Galaxies

With SED models of bright galaxies and density maps in hand, and with structures identified, we match our

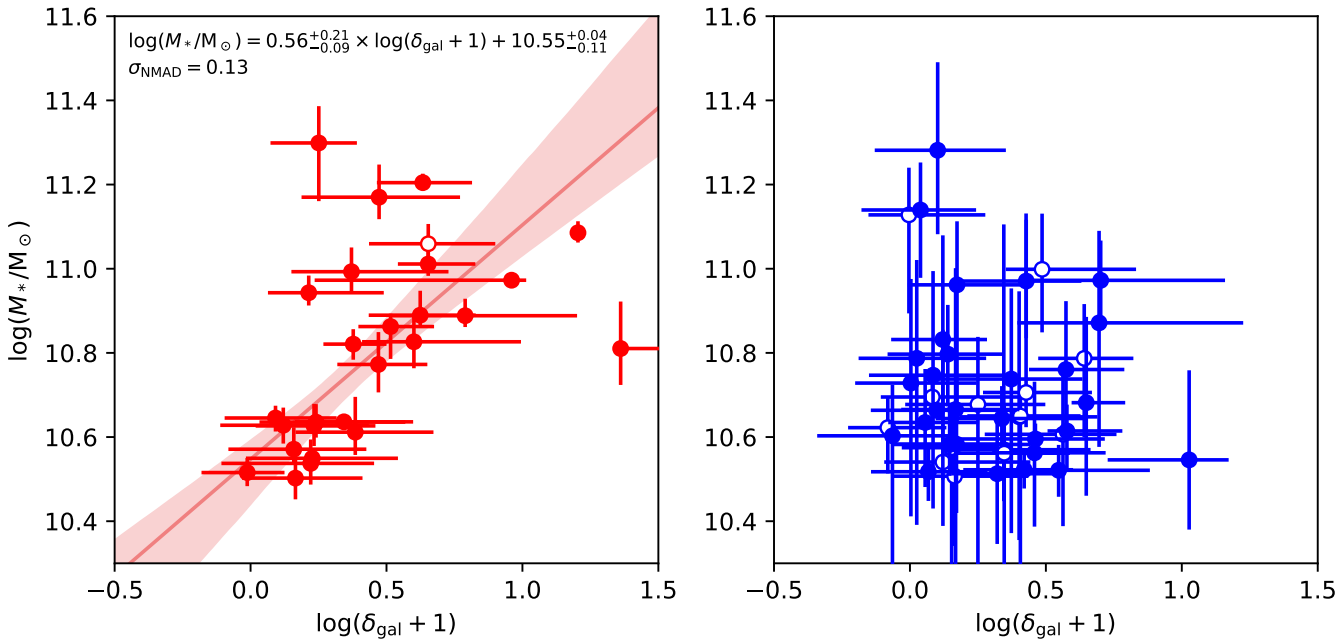


Figure 7. Left: stellar mass as a function of $\log(\delta_{gal} + 1)$ for MQGs (open circles correspond to properties inferred from modeling just photometry). The red line shows the best-fit line to the MQG population using orthogonal distance regression, and the semitransparent bands show the 1σ confidence limits. The best-fit line and the scatter σ_{NMAD} are shown in the top of the panel. Right: same as the left panel, but for the MSFG population. We do not fit a line to the MSFG population due to its higher uncertainties on $\log(M_*/M_\odot)$, though we do note that there seems to be a visually flat or negative relation between stellar mass and local overdensity.

spectroscopy and SED models to the density maps. Sources with spectroscopic redshifts (including bright galaxies for which we have SED models) are assigned local δ_{gal} based on the nearest voxel in the density grid. In Figure 7, we show $\log(\delta_{gal} + 1)$ versus stellar mass for massive galaxies (red for MQGs, blue for MSFGs). For MQGs, we fit a line to these quantities using an orthogonal distance regression (ODR) fit to account for the uncertainties on $\log(\delta_{gal} + 1)$ and the inferred stellar population properties (light red, with the confidence band showing the 1σ uncertainties; the best-fit line and σ_{NMAD} are reported in the top of the panel). The positive trend from the ODR fit visually agrees with the data.

Due to generally higher uncertainties on the inferred stellar mass in the MSFG population, we do not fit a trend line. A simple visual comparison between the two clearly shows that the ODR fit to the MQG sample would be a poor fit for the MSFGs. Instead, there seems to be a flat or negative relation between stellar mass and local overdensity for the star-forming galaxies.

While the locations of the MQGs shown in Figure 5 indicate that they generally lie in or near overdense regions, this is not entirely unexpected. Massive galaxies are biased tracers of cosmic structure, and more overdense regions have more massive halos and, therefore, more massive galaxies. We see this trend for MQGs, where higher masses coincide with higher density values. For MSFGs, however, the trend appears to be reversed or nonexistent, which *is* unexpected. This could indicate an increased efficiency for quenching of massive galaxies in overdense regions. Future analyses studying differences in the SMF between overdense structures and the field will determine if this is the case (e.g., R. F. J. van der Burg et al. 2020; A. H. Edward et al. 2024; B. Forrest et al. 2024).

5.2. Where Massive Galaxies Live

With the identified structures in the EGS and UDS fields and our sample of massive galaxies, we aim to investigate how these populations of massive quiescent and star-forming galaxies are distributed within these structures. To do so, we match each galaxy with its nearest 5σ overdensity down to $\log(M_{Peak}/M_\odot) = 12$. For a given galaxy, we measure the comoving distance from the galaxy to the contour shell enclosing the $5\sigma_{\log(\delta_{gal}+1)}$ peak, $D_{5\sigma}$ (galaxies which lie within the peak have $D_{5\sigma} = 0$). We identify galaxies either within the volumes enclosed by the $5\sigma_{\log(\delta_{gal}+1)}$ peaks or located nearby, within $0 < D_{5\sigma} \leqslant 2.5$ of the peak's border.

Next, we consider the massive galaxy sample. Of the massive galaxies for which the posterior median $\log(M_*/M_\odot) \geqslant 10.5$, we find, as expected, that a higher fraction of these sources are located within $5\sigma_{\log(\delta_{gal}+1)}$ overdensities than of the overall $m_{f444w} < 27.5$ spectroscopic population. However, the uncertainties for quantities inferred from SED modeling like sSFR, SFR, and mass are nonnegligible (especially for dusty star-forming galaxies; see Figure 3), and these quantities are often degenerate. In Figure 3, one can see that the mass uncertainties of several "massive" star-forming galaxies extend far into the lower-mass region, and sSFRs from quiescent and star-forming galaxies cross the $\log(\mathrm{sSFR}/\mathrm{yr}^{-1}) = -10$ line.

Therefore, instead of universally considering a galaxy as "quiescent" or "star-forming," we instead incorporate the uncertainties from their inferred posteriors. We show two-dimensional histograms of the stacked posteriors in sSFR, stellar mass, and dust optical depth in Figure 3 for all 470 galaxies fit with `Prospector` (282 spectrophotometric fits and 188 photometric fits). For each galaxy, we perform 500 random draws from its posterior, reclassifying it as massive quiescent, massive star-forming, or low mass (and rejecting it) depending on that draw's stellar mass and SFR.

In Figure 8, we show how these populations depend on the local structure. The trend lines show the fractions of galaxies of a given population that reside within an overdense peak above a given minimum peak mass. As M_{peak} is restricted to

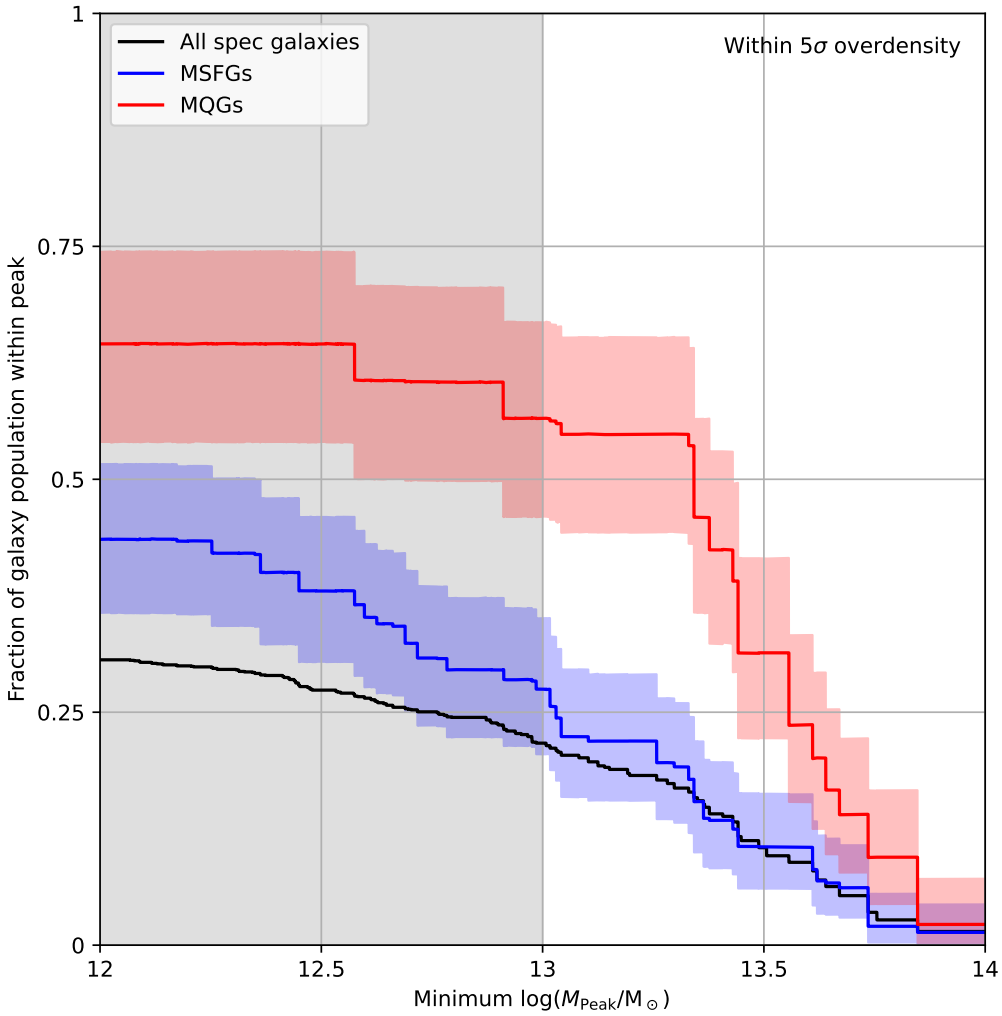


Figure 8. The fractions of spectroscopically confirmed galaxy subpopulations identified within overdense peaks above a minimum $M_{\rm peak}$. As one moves right along the x-axis, the number of overdense peaks above the minimum $\log(M_{\rm Peak}/M_{\odot})$ declines, and therefore the fractions of galaxies within these peaks also decline. We show MQGs (red), MSFGs (blue), and the overall spectroscopic sample (black). Not only are a higher fraction of MQGs found within overdense peaks than any other subpopulation, ∼50% also are found primarily in robustly detected $\log(M_{\rm Peak}/M_{\odot}) \geqslant 13$ overdense peaks. We show all peaks down to $\log(M_{\rm Peak}/M_{\odot}) = 12$, though the peaks in the shaded region $12 \leqslant \log(M_{\rm Peak}/M_{\odot}) < 13$ tend to be physically smaller, with fewer spectroscopically confirmed galaxies, and typically have lower median and maximum density.

higher masses, the fractions of all populations in close proximity to these peaks fall. This is expected because the number of peaks selected (and the number of galaxies around them) naturally decreases as the minimum $\log(M_{\rm Peak}/M_{\odot})$ increases.

However, we see that the relative declines in these populations are remarkably different. At first, the fractions of MSFGs and MQGs within such structures are fairly close for all $\log(M_{\rm Peak}/M_{\odot}) \geqslant 12$ and lie above the overall spectroscopic sample. As the $\log(M_{\rm Peak}/M_{\odot})$ minimum increases, the fraction of MSFGs decreases more rapidly than that of MQGs, with 25% (50%) of massive star-forming (quiescent) galaxies found within robustly detected $5\sigma_{\log(\delta_{\rm gal}+1)}$ peaks with $\log(M_{\rm Peak}/M_{\odot}) \geqslant 13$. A Kolmogorov–Smirnov test comparing the $\log(M_{\rm Peak}/M_{\odot})$ of MSFGs and MQGs returns $p < 0.05$, indicating that the distribution of star-forming and quiescent galaxies in overdense structure is statistically different.

To investigate trends with stellar mass, we consider galaxies with $10 \leqslant \log(M_{*}/M_{\odot}) < 10.5$ (which may suffer from mass incompleteness) and break down the massive $\log(M_{*}/M_{\odot}) \geqslant 10.5$ sample into two mass bins of roughly equal bulk posterior mass: $10.5 \leqslant \log(M_{*}/M_{\odot}) < 10.75$ and $\log(M_{*}/M_{\odot}) \geqslant 10.75$. We show how the star-forming and quiescent subpopulations of these sets depend on $\log(M_{\rm Peak}/M_{\odot})$ in the top row of Figure 9. In the bottom row, we show the region "nearby" the peak (within 2.5 cMpc of the border). In most panels, quiescent galaxies and star-forming galaxies are indistinguishable from the spectroscopic population, but in the top-right panel, a significantly higher fraction of $\log(M_{*}/M_{\odot}) \geqslant 10.75$ quiescent galaxies is found in overdense peaks than in the general spectroscopic population or even star-forming galaxies of similar mass.

5.3. Quiescent Fractions

To investigate whether the evolution of massive galaxies in overdense regions differs from that in the coeval field, we compare quiescent fractions $f_Q = N_{\rm Q}/(N_{\rm SF} + N_{\rm Q})$ across different stellar masses and environments. We separate all modeled galaxies into two sets: Galaxies with $\log(\delta_{\rm gal} + 1) > 5\sigma_{\log(\delta_{\rm gal}+1)}$ are flagged as overdensity galaxies and those with $\log(\delta_{\rm gal} + 1) < 3\sigma_{\log(\delta_{\rm gal}+1)}$ are flagged as

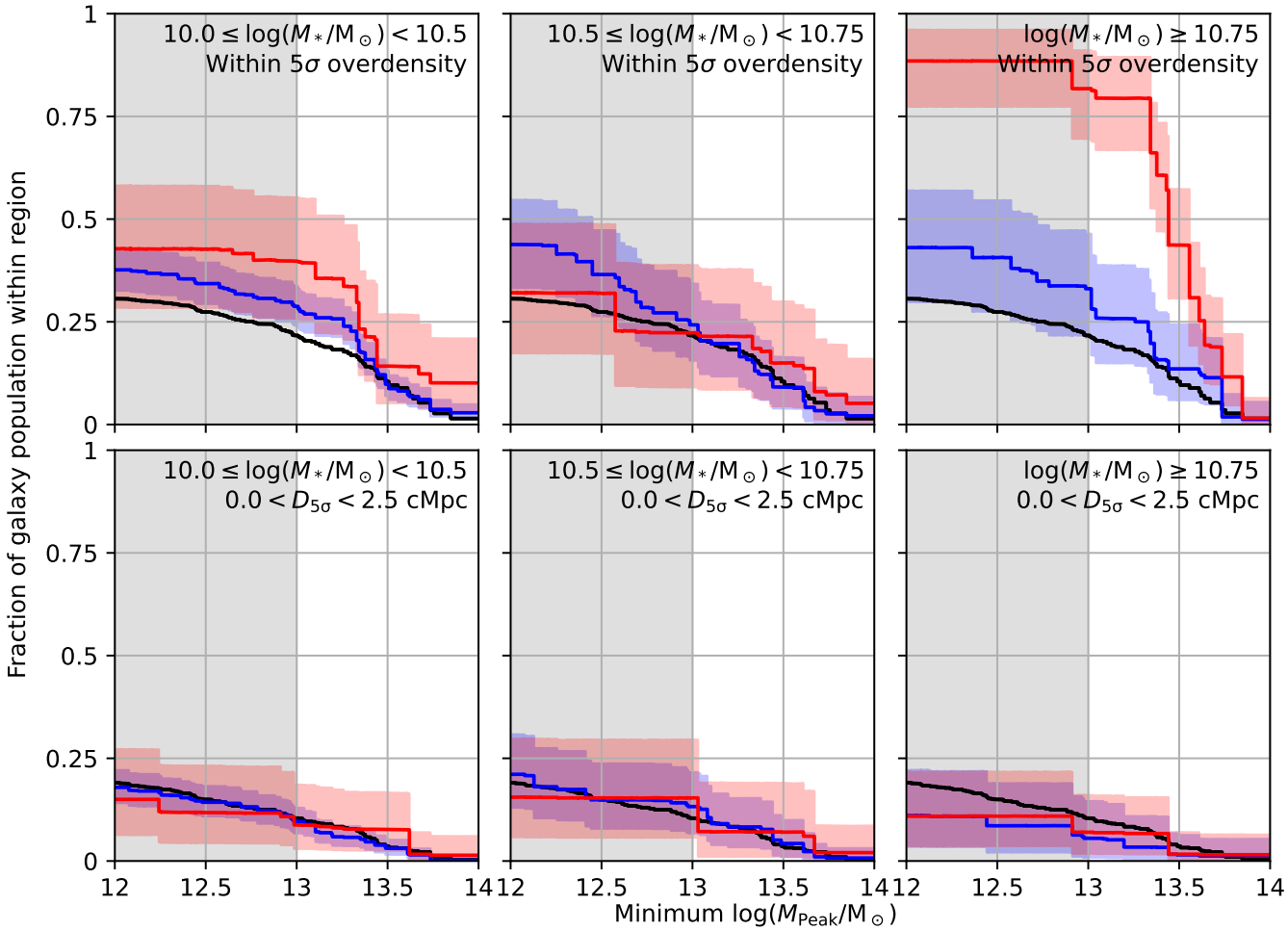


Figure 9. Same as Figure 8, but splitting MQGs and MSFGs into different stellar mass bins (low to high, left to right) and different regions (top to bottom, inside overdense peak versus immediately nearby overdense peak). The black line representing all spectroscopically confirmed galaxies is uniform across the mass bins. At lower stellar masses, the clustering of MQGs and MSFGs is indistinguishable from the overall spectroscopic sample; at higher stellar masses, however, MQGs appear to cluster much more strongly in overdense peaks.

coeval field galaxies. We calculate the quiescent fractions of these subpopulations as functions of both $M_{\rm peak}$ and galaxy stellar mass.

In the left panel of Figure 10, we show the f_Q of overdensity galaxies in red as a function of the $M_{\rm peak}$ of their local overdensity. The field sample is shown as a blue line. In this panel, we restrict the sample to galaxies with $\log(M_*/M_\odot) \geqslant 10.5$. In the right panel, we show the f_Q of our modeled spectroscopically confirmed galaxies, where the overdensity population (red) is limited to $\log(M_{\rm peak}/M_\odot) \geqslant 13$. The grayed regions in each panel indicate the mass regime excluded in the other (though including them does not change the observed trends). In both panels, we show the median f_Q as a solid colored line (when the median $N_{\rm Q} + N_{\rm SF} < 5$, the line is dashed to indicate sparsely populated regions of parameter space) and the 1σ uncertainties as the filled regions.

Previous studies of quiescent galaxies and their environments have highlighted individual $z \gtrsim 3$ structures with elevated quiescent fractions and have suggested that environmental quenching may play a role in MQG evolution (e.g., K. Shi et al. 2021; I. McConachie et al. 2022; K. Ito et al. 2023; M. Tanaka et al. 2024; I. McConachie et al. 2025; N. B. Sillassen et al. 2026). Our results qualitatively match these trends; we find that in larger and more overdense structures, higher fractions of massive galaxies are quiescent than in the coeval field, and this trend appears to be dependent on galaxy stellar mass. We see tentative evidence for higher $f_{\rm Q}$ in the field at extremely high stellar mass; however, uncertainties in this regime are dominated by Poisson statistics. In an analysis of small-scale overdensities in COSMOS, T. Kakimoto et al. (2026b) examined quenched fractions in different stellar mass, environment, and redshift bins. They observe a similar trend at $3.2 < z < 5$, where $f_{\rm Q}$ is generally higher both at high overdensity $\delta_{\rm gal}$ and at high stellar mass M_*.

The lack of an elevated $f_{\rm Q}$ at low stellar mass suggests that the environmental quenching mechanisms typically thought to be responsible for quenching this population in low-redshift clusters are not yet dominant at high z (R. Pan et al. 2025; T. Kakimoto et al. 2026b). At high stellar mass and high redshift, internal processes associated with "mass quenching" (such as AGN feedback; e.g., L. Xie et al. 2024) are thought to dominate. In an investigation of high-z quenching in the GAEA semianalytical model, L. Xie et al. (2024) found that AGN feedback triggered by mergers is the dominant driver in quenching $\log(M_*/M_\odot) \gtrsim 10.7$ galaxies. As local overdensity has been shown to elevate both merger fractions (e.g., N. K. Hine et al. 2016; S. Liu et al. 2023; T. Shibuya et al. 2025) and AGN fractions (e.g., B. D. Lehmer et al. 2009; C. Gatica et al. 2023; A. Travascio et al. 2025), this offers a

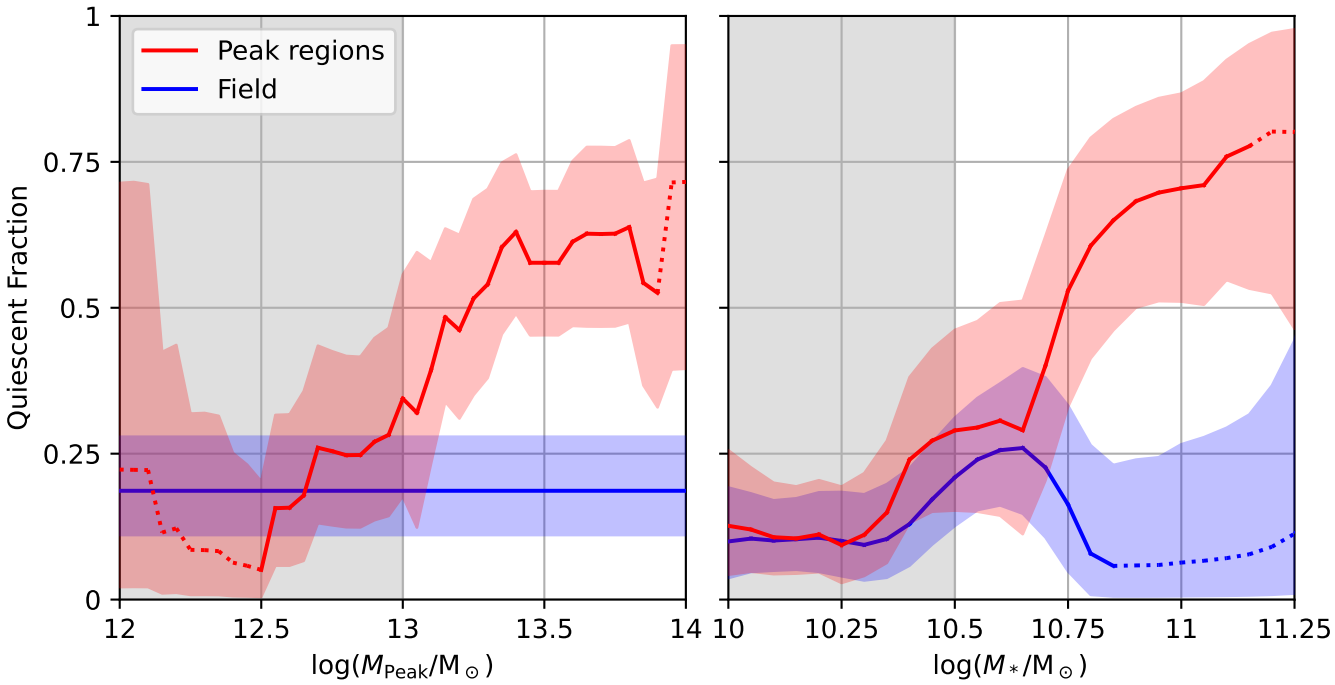


Figure 10. Left: the quiescent fraction of $\log(M_*/M_\odot) \geqslant 10.5$ spectroscopically confirmed galaxies in overdense peaks as a function of overdense peak $M_{\rm peak}$ is shown in red. In blue, we show the quiescent fraction of $\log(M_*/M_\odot) \geqslant 10.5$ galaxies in the field ($\log(\delta_{\rm gal}+1) < 3\sigma_{\log(\delta_{\rm gal}+1)}$). Right: quiescent fractions of galaxies in overdense peaks with $\log(M_{\rm Peak}/M_\odot) \geqslant 13$ are shown as a function of galaxy M_*. In both panels, the gray shaded region indicates the part of parameter space not included in the other panel. Quiescent fractions in both cases are calculated in a moving window 0.5 dex wide. The solid median line is replaced with a dashed line when the total number of galaxies in the bin $N_{\rm SF} + N_{\rm Q} < 5$.

plausible explanation for the difference in quiescent fractions we see between overdense regions and the field.

6. Discussion

The fact that MQGs preferentially are found in overdense peaks and quiescent fractions are higher in overdense peaks points toward more efficient quenching in these environments. However, we find that overdensity MQGs also tend to be more massive, which could suggest more efficient and rapid mass assembly in overdense regions than the field at these early cosmic times. To investigate the potential effects of environment on MQG formation, we use the inferred SFHs from `Prospector` to estimate the stellar mass of MQG progenitors at $z > 5$ using different basic mass assembly models and draw comparisons with observations and simulations. In this test, we include 33 of 35 spectrophotometrically modeled quiescent galaxies (red models in Figures 1 and A1), excluding DeepDive-38239 and RUBIES-55077 for their poor coverage of the Balmer break and therefore poorly constrained SFHs.

6.1. Mass Assembly History Models

In the first model of mass assembly, the single-halo progenitor (SHP), we assume all stellar mass originates in the progenitor's halo. Because all of the stars are assumed to form in situ, the SFH perfectly traces the stellar mass growth of the progenitor.

For the second model of mass assembly, we allow the main progenitor (i.e., the most massive progenitor) to assemble mass via major mergers with nearby galaxies. The growth of the progenitor is therefore dictated by both its SFR (in situ) and its mass-accretion rate (MAR; ex situ), the average amount of stellar mass added per unit time from mergers.

The MAR is not quantifiable from SED fitting alone, so we use a parameterization from the literature. By counting pairs in JWST Cycle 1 NIRCam imaging, Q. Duan et al. (2025) fit power-law and power-law plus exponential models to merger fractions and MARs at $z > 4.5$. We adopt their power-law parameterization of the specific MAR (sMAR), while also cautioning that their results appear to be primarily driven by the lower end of their stellar mass range at $8 < \log(M_*/M_\odot) < 10$ and that the major merger fraction $f_{\rm merger}$ does appear to depend on M_* (see their Figure 5b; their use of the term pair fraction $f_{\rm p}$ is equivalent to the merger fraction). For a given quiescent galaxy, we assume that the sSFR is the same across all of its progenitor halos. Then, we calculate the stellar mass of the most massive progenitor galaxy $M_{*,\rm primary}(t)$ at cosmic time $t < t_{\rm obs}$ from the total stellar mass in the SFH at that time $M_{*,\rm tot}(t)$ by correcting for the existing stellar mass which has formed in other halos by time t and has not yet accreted onto the main progenitor:

$$M_{*,\rm primary}(t) = M_{*,\rm tot}(t) \cdot e^{-f(t)}, \tag{2}$$

$$M_{*,\rm primary}(t) = M_{*,\rm tot}(t) \cdot e^{-f(t)}. \tag{3}$$

Spreading the formed stellar mass across multiple progenitor halos decreases the stellar mass of the main progenitor by up to an order of magnitude at $z \sim 10$. R. K. Cochrane (2025) found similar correction offsets for particularly massive and old galaxies in an analysis of the effects of ex situ star formation on inferred stellar mass growth histories in TNG-100. With $M_{*,\rm primary}$, we can calculate the ex situ fraction:

$$f_{\rm ex\text{-}situ} = \frac{M_{*,\rm ex\text{-}situ}}{M_{*,\rm formed}}, \tag{4}$$

$$M_{*,\mathrm{ex\text{-}situ}} = \int_0^{t_{\mathrm{obs}}} M_{*,\mathrm{primary}}(t) \cdot \mathrm{sMAR}(t) \cdot dt, \quad (5)$$

where $M_{*,\mathrm{formed}}$ is the total stellar mass formed in the inferred SFH. We find, perhaps counterintuitively, that often the fraction of MQG stars that formed ex situ is fairly low. The fraction f_{exsitu} is typically only about 0.1–0.3 for most MQGs, but can vary as high as 0.5–0.7 for a few outliers that are particularly massive and formed early (e.g., RUBIES-EGS-QG1, EXCELS-109760, and ZF-UDS-7329), which qualitatively matches the trends with stellar mass seen in F. Huško et al. (2022) and D. Puskás et al. (2025).

Finally, in the third model, we introduce a δ_{gal}-dependent multiplicative factor to the sMAR account for a higher/lower number of potential merger partners in more/less dense environments. In an analysis of $z \sim 2$–5 pairs in the HSC-SSP, T. Shibuya et al. (2025) showed that the merger fraction f_{merger} exhibits a positive correlation with local overdensity that appears to be redshift invariant (at least out to $z \sim 5$). They find a galaxy merger fraction enhancement ratio $R_{\mathrm{merger}}(\delta) = f_{\mathrm{merger}}(\delta)/f_{\mathrm{merger}}(\delta = 0) = 0.15 \cdot \delta + 0.97(^{+0.36}_{-0.31})$. As sMAR is linearly proportional to the merger fraction f_{merger}, we apply a similar scaling to the sMAR. Because Q. Duan et al. (2025) effectively marginalized over δ_{gal}, we assume their $f_{\mathrm{merger}} = f_{\mathrm{merger}}(\mathrm{median}(\delta_{\mathrm{gal}}))$, where $\mathrm{median}(\delta_{\mathrm{gal}}) \approx 1.25$ for $\log(M_*/M_\odot) \geqslant 10.5$ galaxies (the assumed descendants of the proposed mergers). We additionally reduce the constant multiplied by δ_{gal} from 0.15 to 0.05 to conservatively hedge against underestimated overdensity measurements from photometric redshifts in T. Shibuya et al. (2025). Our δ_{gal}-dependent sMAR is thus

$$\mathrm{sMAR}(\delta_{\mathrm{gal}}, t) = [0.05 \cdot (\delta_{\mathrm{gal}} - 1.25) + 1] \cdot \mathrm{sMAR}(t), \quad (6)$$

which can then be used to recompute $M_{*,\mathrm{primary}}(t)$ from Equation (2).

6.2. Comparison with Stellar Mass Function

To compare these mass assembly models with high-redshift observations, we integrate the Schechter function fit to the galaxy SMF in A. Weibel et al. (2024) between $10.0 < \log(M_*/M_\odot) < 12$ and $10.5 < \log(M_*/M_\odot) < 12$ in an equivalent comoving volume to that spanned by our spectroscopic sample at $3 < z < 5$ in the UDS and EGS (≈333 arcmin^2 total). We perform this for the $z \sim 5$, $z \sim 6$, and $z \sim 7$ SMFs (measured in redshift bins $4.5 < z < 5.5$, $5.5 < z < 6.5$, and $6.5 < z < 7.5$). Because the integral is strongly dependent on $\log(M^*)$, which is anticorrelated with $\log(\Phi^*)$ and α, the uncertainties we obtain from bootstrapping are likely *over*-estimated in the $z \sim 5$ and 6 bins; in the $z \sim 7$ bin, A. Weibel et al. (2024) fixed $\log M^* = 10$, so uncertainties here could be *under*estimated. The number of galaxies N_{gal} in this stellar mass range expected in this volume is shown as black squares in Figure 11.

We count the number of $\log(M_*/M_\odot) > 10.0$ and $\log(M_*/M_\odot) > 10.5$ progenitors at $4.5 < z < 7.5$ and obtain measurement uncertainties by bootstrapping draws from the posteriors. The red line/dark band/light band show the median/$1\sigma/2\sigma$ confidence bands on the number of MQG SHPs in Figure 11 (top row). While the number of $\log(M_*/M_\odot) > 10.0$ SHPs at high redshift agrees with the number of such massive galaxies obtained from the observed SMF, at $\log(M_*/M_\odot) > 10.5 N_{\mathrm{gal}}$ the number of SHPs is markedly higher than N_{gal} from the SMF. In other words, single progenitors formed according to the inferred SFHs would be significantly more massive and numerous at $z > 5$ than actual, observed high-redshift galaxies. The green line and confidence bands in the second row of Figure 11 show the results from the allowed merger accretion model. By allowing for merger-driven growth, the main quiescent galaxy progenitors' masses are decreased and their inferred numbers are less in conflict with the observed SMF. Further introducing a dependence on local environment (blue, third row) brings the number of $\log(M_*/M_\odot) > 10.5$ progenitors into 2σ agreement with the observed SMF at the high-z end.

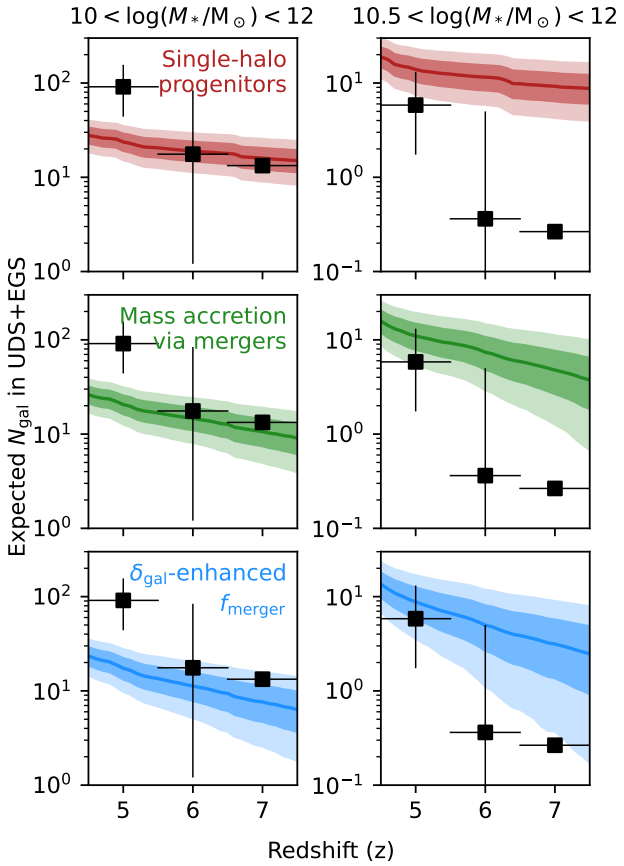


Figure 11. Expected numbers of $10 < \log(M_*/M_\odot) < 12$ (left) and $10.5 < \log(M_*/M_\odot) < 12$ (right) galaxies at $z = 5$, 6, and 7 from the integrated galaxy SMF in A. Weibel et al. (2024; black squares) and the SFHs of the MQGs in this work under different stellar mass assembly assumptions (colored bands; the line shows the median, and dark/light bands show $1\sigma/2\sigma$ confidence intervals). In the first case (red), we assume all of a quiescent galaxy's stellar mass is formed in situ in a single progenitor halo. Above the knee of the SMF ($\log(M_*/M_\odot) > 10.5$), the number of expected MQG progenitors far exceeds the observed number counts. The green band shows the number counts of primary quiescent galaxy progenitors under the assumption that all primaries grow via mergers, quantified by a redshift-dependent specific mass-accretion rate (Q. Duan et al. 2025). Finally, the blue band shows how introducing a dependence on local environment δ_{gal} to the merger fraction (and therefore the sMAR) further reduces the inferred number of high-mass primary progenitors and produces better agreement with high-z observations.

6.3. Comparison with High-z Simulated MQGs

Next, we turn to high-redshift simulations of quiescent galaxies. H. G. Chittenden et al. (2026) identified nine $\log(M_*/M_\odot) > 10$ galaxies in the THESAN-1 simulation box (side length 95.5 cMpc) with sSFR $< 1\mathrm{Gyr}^{-1}$ at $z = 5.5$

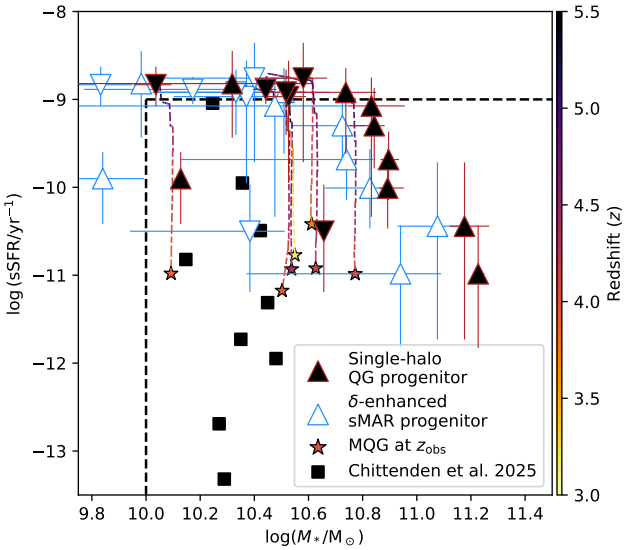


Figure 12. A comparison of the 15 quiescent galaxy single-halo progenitors (black triangles with red outlines; upright triangles denote overdensity MQG progenitors, downturned triangles are field MQG progenitors) with $\log(M_{*,84}/M_\odot) > 10$ and $\log(\mathrm{sSFR}_{16}/\mathrm{yr}^{-1}) < -9$ at $z = 5.5$ with the nine simulated quiescent galaxies from the THESAN simulation (H. G. Chittenden et al. 2026; black squares). Blue-outlined white triangles show the MQG progenitor population when mergers are allowed and enhanced by δ_{gal}. Of the eight MQG SHPs with median stellar mass and sSFR in the quiescent region (black dashed square), seven are found in overdensities. MQG SHPs often have either higher stellar masses or sSFRs compared to the simulated quiescent galaxies. The density-enhanced merger model progenitors are lower mass than the SHPs, but in the most extreme cases are still more massive than the simulated quiescent galaxies in THESAN.

(black squares in Figure 12). To compare with these findings, we trace back the SFHs of the 33 $\log(M_*/M_\odot) \geqslant 10$ quiescent galaxies and examine their total stellar mass and sSFR at $z = 5.5$. For the subset of $z = 5.5$ quiescent galaxy SHPs which lie within 1σ of the quiescent region, we show their total stellar masses and sSFRs $z = 5.5$ as triangles with red borders (upright triangles for overdensity quiescent galaxies and inverted triangles for field quiescent galaxies) in Figure 12. Median SFHs are shown as colored dashed lines terminating in stars colored by z_{obs} for quiescent galaxies whose $z = 5.5$ medians lie outside the quiescent box to show their projected growth; $z = 5.5$ quiescent galaxy progenitors already inside this region do not experience much mass evolution and typically only move vertically down.

The $z = 5.5$ quiescent galaxy SHPs tend to occupy different regions of parameter space from the simulated $z = 5.5$ quiescent galaxies; most have higher stellar masses and/or higher sSFRs. We show the $z = 5.5$ progenitor population allowing for δ_{gal}-enhanced merger fractions as open blue triangles. This mass assembly model lessens the conflict with the simulated quiescent galaxies, but these progenitors are still half an order of magnitude too massive, and their sSFRs are unchanged. We speculate that this latter disagreement could be improved by changing the sSFR across progenitor halos. Increasing ex situ star formation by forming more stars in nonprimary halos would lower the sSFR in the primary and could feasibly bring some of the blue triangles along the top of the quiescent box in Figure 12 down toward the simulated $z = 5.5$ quiescent galaxies. However, such an effect would also increase the number of quiescent galaxies at high redshift, which has already been shown to agree well with observations (Y. Zhang et al. 2026b). Accounting for color gradients (e.g., S. E. Cutler et al. 2026) or α-enhanced stellar populations (e.g., M. Park et al. 2025; M. L. Hamadouche et al. 2026; H. H. Leung et al. 2026; I. McConachie et al. 2026) has been found to lower the inferred stellar mass and/or age, so we suggest that these in combination with growth via mergers could further reduce the tension between the inferred SFHs of MQGs and simulations and observations at high redshift.

6.4. Caveats and Takeaways

Observationally constraining the previous mass assembly of individual high-redshift galaxies is challenging. In this work, we applied a simplistic density-dependent mass accretion model to a population of spectroscopically confirmed quiescent galaxies, but there are still several significant caveats. A nonexhaustive list follows. Because of the low number density of galaxies at the high-mass end of the SMF, high-z pair studies are statistically limited to galaxies at considerably lower stellar masses than the MQGs; pair fractions and major (and minor) merger rates at the high-mass end are therefore poorly constrained. The evolution of the role of environment in the merger fraction at $z > 5$ is similarly poorly constrained. We assume the observed δ_{gal} does not evolve with redshift, which is unphysical. We were able to analytically solve for the progenitor's $M_*(z)$ by setting sSFR equal across all of a quiescent galaxy's progenitor halos; however, this assumption is not physically motivated.

Despite these broad assumptions, we find that the mass assemblies inferred are not wildly out of line with other studies investigating mergers in observations or simulations. As discussed in Section 6.1, ex situ fractions and the change in progenitor mass are consistent with other studies. Therefore, although the analytical merger models considered here are simplistic and based on high-redshift pair fractions, we argue that this agreement qualitatively supports the application of these models to the observed $3 < z < 5$ quiescent galaxy population.

In Sections 6.2 and 6.3, we demonstrated that if all of the stars in the inferred SFHs of MQGs formed in single halos, these high-z progenitors would be too massive for either observations or simulations at high redshift. We then showed that by offloading star formation from the primary progenitor halo into neighboring halos that merge with the primary at later cosmic times, this tension can be lessened. Although we cannot robustly quantify the contribution of mergers to MQG assembly, these examples offer additional evidence that hierarchical assembly and local environment play an important role in the formation and evolution of high-redshift MQGs.

7. Conclusions

In this paper, we presented an analysis of the environments of massive galaxies in the EGS and UDS fields using RUBIES spectroscopy and archival data from the DJA. We summarize our findings below.

1. Using a MCVT technique to combine photometry and over 2000 spectroscopic redshifts in the UDS and EGS fields, we produce galaxy overdensity maps and identify 19 overdense peaks containing massive galaxies at $3 < z < 5$ and seven protoclusters.
2. We investigate how stellar mass trends with environment $\log(\delta_{\mathrm{gal}} + 1)$ for MQGs and MSFGs. As might be expected from hierarchical structure formation, we

observe a positive trend between MQG stellar mass and overdensity; however, this trend is curiously absent from the MSFG population. This could suggest an increased efficiency of quenching mechanisms in overdense environments.

3. We find that massive galaxies cluster strongly (again, as would be expected from hierarchical structure formation): A high fraction (≈30%) live within massive ($\log(M_{\rm Peak}/M_{\odot}) \geqslant 13$) overdense peaks, with an even stronger preference for quiescent galaxies to lie in such overdensities (≈50%). We explore how this trend depends on stellar mass and proximity to the overdensity, finding that over 75% of $\log(M_*/M_{\odot}) \geqslant 10.75$ quiescent galaxies are located within massive overdense peaks.
4. We calculate quiescent fractions $f_{\rm Q}$ as a function of the inferred mass of the overdense peak $M_{\rm peak}$ and as a function of galaxy stellar mass M_*. We find that at both higher $M_{\rm peak}$ and M_*, $f_{\rm Q}$ in overdense peaks is elevated relative to the coeval field, reproducing trends seen in other observations. We suggest that this pattern demonstrates that the mechanisms responsible for quenching massive galaxies at high z have some dependence on local environment and can be enhanced or triggered more frequently in overdense regions.
5. Using the inferred SFHs from the quiescent galaxy sample, we compare the total mass at $z > 5$ of the observed MQGs with high-redshift observations and simulations. We test three basic mass assembly models, one assuming all stars form in situ, one allowing the progenitor to accrete stellar mass via mergers, and one where the merger rate is further enhanced by $\delta_{\rm gal}$. We find that the single-halo in situ assumption dramatically overestimates the number of $\log(M_*/M_{\odot}) > 10.5$ galaxies at $z > 5$, but by allowing stars to form in neighboring halos and accrete onto the primary at later times, this tension is lessened. Because the most massive MQGs are also found in overdense environments, enhancing the merger fraction and merger rate by $\delta_{\rm gal}$ brings the number of massive progenitors down to 2σ agreement with the observed SMF and lessens (but does not solve) the conflict with the THESAN simulation's quiescent galaxy masses. We argue that these trends indicate that ex situ star formation in overdense environments plays an important role in high-redshift quiescent galaxy assembly.

Acknowledgments

This work is based in part on observations made with the NASA/ESA/CSA James Webb Space Telescope. The data were obtained from the Mikulski Archive for Space Telescopes at the Space Telescope Science Institute, which is operated by the Association of Universities for Research in Astronomy, Inc., under NASA contract NAS 5-03127 for JWST. The observations used in this analysis are associated with program Nos. 1213, 1215, 1345, 2565, 2750, 3543, 3567, 4106, 4233, 4287, 5224, and 6368, and can be accessed at doi:10.17909/cqv0-gx76.

Some of the data products presented herein were retrieved from the Dawn JWST Archive (DJA). DJA is an initiative of the Cosmic Dawn Center (DAWN), which is funded by the Danish National Research Foundation under grant DNRF140.

The authors acknowledge the CEERS and PRIMER teams for developing their observing program with a zero-exclusive-access period. K.G. and T.N. acknowledge support from Australian Research Council Laureate Fellowship FL180100060. Support for programs GO-4233 and GO-3659 was provided by NASA through a grant from the Space Telescope Science Institute, which is operated by the Association of Universities for Research in Astronomy, Inc., under NASA contract NAS 5-03127.

Facilities: HST, JWST.

Software: Matplotlib (J. D. Hunter 2007), NumPy (C. R. Harris et al. 2020), astropy (Astropy Collaboration et al. 2013, 2018; Astropy Collaboration et al. 2022), Prospector (B. Johnson & J. Leja 2017; B. D. Johnson et al. 2021), dynesty (J. S. Speagle 2020), joblib (joblib developers, T. 2025), mayavi (P. Ramachandran & G. Varoquaux 2011). The LLM Google Gemini was used in the formatting of the interactive HTML and X3D files (Figure 6).

Appendix A
Moderate-mass Quiescent Galaxies and Dusty Star-forming Interlopers

This appendix shows the spectra and stellar population properties moderate-mass quiescent galaxies in Figure A1 and Table A1. We also show examples of dusty star-forming interlopers in Figure A2.

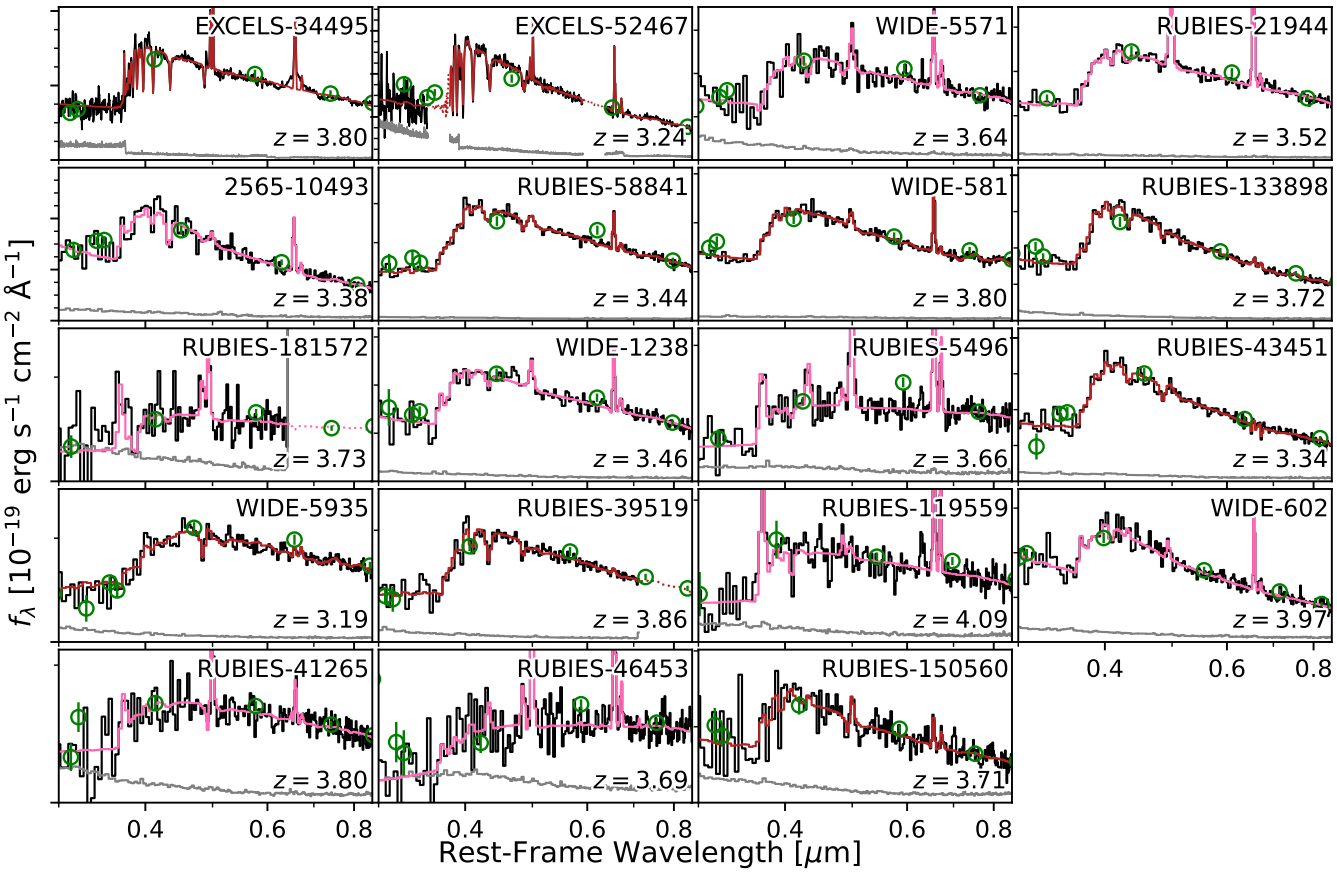


Figure A1. Same as Figure 1, but for moderate-mass $10 \leqslant \log(M_*/M_\odot) < 10.5$ quiescent galaxies and marginally quiescent galaxies.

Table A1
Moderate-mass Quiescent Galaxies

ID	R.A. (deg)	Decl. (deg)	$z_{\rm spec}$	$\log(M_*/M_\odot)$	$\rm SFR_{10Myr}$ ($M_\odot$ yr^{-1})	$\log(\delta_{\rm gal}+1)$	Programs
EXCELS-34495	34.289463	−5.269810	3.796	$10.50^{+0.03}_{-0.03}$	$0.1^{+0.8}_{-0.1}$	$0.83^{+0.25}_{-0.14}$	3, 4
EXCELS-52467	34.344085	−5.239474	3.237	$10.49^{+0.02}_{-0.02}$	$2.2^{+0.7}_{-0.7}$	$0.38^{+0.16}_{-0.13}$	4
WIDE-5571[a]	34.437763	−5.226583	3.644	$10.49^{+0.07}_{-0.07}$	$7.5^{+8.8}_{-5.6}$	$0.18^{+0.22}_{-0.20}$	1
RUBIES-21944[a]	34.469218	−5.283563	3.528	$10.40^{+0.06}_{-0.06}$	$4.6^{+5.2}_{-3.6}$	$0.75^{+0.31}_{-0.17}$	7
2565-10493[a]	34.274382	−5.241174	3.390	$10.40^{+0.04}_{-0.06}$	$2.9^{+6.5}_{-2.7}$	$0.24^{+0.27}_{-0.22}$	3, 4
RUBIES-58841	214.879098	52.888065	3.451	$10.39^{+0.04}_{-0.04}$	$0.1^{+0.2}_{-0.1}$	$1.16^{+0.00}_{-0.00}$	7, 9
WIDE-581	34.282266	−5.244876	3.805	$10.30^{+0.04}_{-0.05}$	$1.1^{+2.8}_{-1.0}$	$0.52^{+0.18}_{-0.20}$	1
RUBIES-133898	34.485164	−5.157813	3.704	$10.25^{+0.04}_{-0.05}$	$1.1^{+2.6}_{-1.0}$	$0.14^{+0.14}_{-0.17}$	3, 7
RUBIES-181572[a]	34.417824	−5.089469	3.779	$10.24^{+0.13}_{-0.19}$	$8.1^{+13.3}_{-6.7}$	$-0.08^{+0.20}_{-0.18}$	7
WIDE-1238[a]	215.011053	52.908065	3.455	$10.21^{+0.05}_{-0.05}$	$3.1^{+3.9}_{-2.6}$	$0.40^{+0.42}_{-0.23}$	1
RUBIES-5496[a]	34.405872	−5.312951	3.662	$10.21^{+0.12}_{-0.19}$	$4.8^{+10.2}_{-4.0}$	$0.04^{+0.27}_{-0.20}$	7
RUBIES-43451	214.909553	52.875028	3.340	$10.14^{+0.03}_{-0.02}$	$0.3^{+0.6}_{-0.3}$	$0.20^{+0.16}_{-0.16}$	7
WIDE-5935	34.254473	−5.234889	3.207	$10.11^{+0.01}_{-0.02}$	$1.0^{+0.2}_{-0.2}$	$0.56^{+0.26}_{-0.19}$	1, 3, 4, 7
RUBIES-39519	34.404697	−5.254782	3.873	$10.09^{+0.05}_{-0.04}$	$0.1^{+0.4}_{-0.1}$	$0.14^{+0.16}_{-0.19}$	7
RUBIES-119559[a]	34.304860	−5.177419	4.088	$10.08^{+0.09}_{-0.09}$	$2.5^{+5.9}_{-2.1}$	$0.07^{+0.19}_{-0.21}$	7
WIDE-602[a]	34.467800	−5.244913	3.965	$10.07^{+0.05}_{-0.05}$	$1.6^{+3.0}_{-1.5}$	$0.06^{+0.24}_{-0.23}$	1,7
RUBIES-41265[a]	34.357466	−5.252228	3.784	$10.05^{+0.07}_{-0.13}$	$2.2^{+3.9}_{-1.9}$	$0.61^{+0.26}_{-0.28}$	7
RUBIES-46453[a]	34.259690	−5.234624	3.698	$10.04^{+0.14}_{-0.27}$	$3.5^{+11.1}_{-3.3}$	$0.42^{+0.18}_{-0.13}$	7
RUBIES-150560	34.436214	−5.135380	3.719	$10.00^{+0.04}_{-0.04}$	$0.9^{+1.2}_{-0.8}$	$-0.03^{+0.20}_{-0.18}$	7

Notes. Same as Table 1. We do not list the eight marginally quiescent photometric fits here. In the "Programs" column, we list the programs that obtained spectra of each galaxy, ordered numerically by program ID: (1) 1213/1215, WIDE (M. V. Maseda et al. 2024); (2) 1345, CEERS (S. L. Finkelstein et al. 2023); (3) 2565 (T. Nanayakkara et al. 2024; T. Nanayakkara et al. 2025); (4) 3543, EXCELS (A. C. Carnall et al. 2024; H. H. Leung et al. 2026); (5) 3567, DeepDive (M. L. Hamadouche et al. 2026; K. Ito et al. 2026); (6) 4106 (PI: E. Nelson); (7) 4233, RUBIES (A. de Graaff et al. 2025b; Y. Zhang et al. 2026a); (8) 5224, Mirage or Miracle (PI: P. Oesch); (9) 6368, CAPERS (PI: M. Dickinson).

[a] Marginally quiescent with $\log(\rm sSFR_{16}/yr^{-1}) < -10$, not included in Sections 6.2 or 6.3. Most moderate-mass marginally quiescent galaxies have large SFR uncertainties.

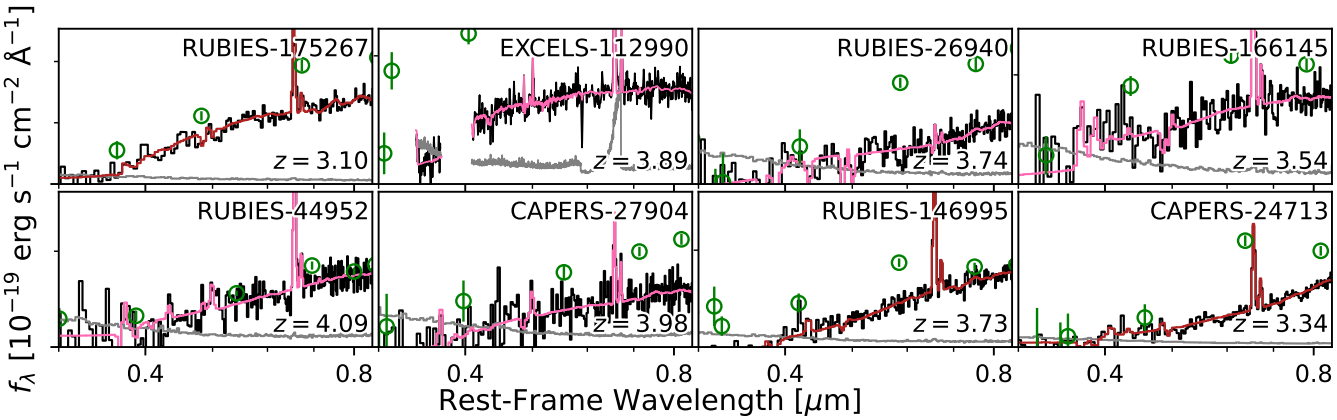


Figure A2. Eight NIRSpec spectra (black) and best-fit `Prospector` models for galaxies with $\log(M_*/M_\odot) \geqslant 10.5$, $\tau_{\rm dust} \geqslant 1.5$, and either $\log(\mathrm{sSFR}/\mathrm{yr}^{-1}) < -10$ (red) or $\log(\mathrm{sSFR}_{16}/\mathrm{yr}^{-1}) < -10$ (pink). Unlike Figures 1 and A1, here we leave the spectra uncalibrated and show the model spectrum scaled to the observed instead. Based on their high dust optical depths, we classify them as "dusty star-forming galaxies" by default, though classifying them as quiescent leaves our conclusions unchanged.

Appendix B
Monte Carlo Voronoi Tessellation

B.1. Ingredients

This subsection describes the three input data products. The two-dimensional field grid is the plane that we will partition into cells centered on galaxies (i.e., Voronoi tessellation), the coordinates of which are taken from the source coordinate catalog if their entry in the redshift catalog indicates that they are members of the redshift slice.

B.1.1. Field Grid

First, we construct a grid of pixels upon which we will perform the Voronoi tessellation. Before we begin our density estimation method, we adjust our coordinate system for geometric convenience. Because the UDS is an equatorial field, the angular distance between two sources within it will be fairly close to a Cartesian approximation with R.A. and decl. as x and y coordinates (a difference of $<0.01\%$). This approximation, however, cannot be made in the EGS, which lies at decl. $\sim$53, where separation is very non-Cartesian due to spherical geometry.

To ameliorate the effects of spherical geometry, we reorient our coordinate axes. We take the median R.A. and decl. in each of the photometric catalogs to be the "center" of each field and apply an invertible transformation to our coordinate frame that places the center at the origin while preserving angular separations. We refer to these new axes as R.A.′ and decl.′ Finally, for computational efficiency, in the case of the EGS, we rotate our axes by 49 degrees counterclockwise such that the field lies flat along the R.A.′ axis (in the UDS, which is left unrotated, R.A.′ and decl.′ are equivalent to ΔR.A. and Δdecl.). Because our fields are equatorial in R.A.′ and decl.′, we therefore perform our analyses using a Cartesian approximation in these coordinates, which is a good approximation of the angular separation in R.A. and decl.

On top of the field in R.A.′ and decl.′, we overlay a Cartesian grid of $2\farcs5 \times 2\farcs5$ pixels that extends $5'$ beyond the field edges in each direction (each pixel $\mathrm{R.A.}'_i$, $\mathrm{decl.}'_j$ can easily be translated back to traditional R.A. and decl. coordinates using the inverse transformation). Using the F444W mosaics from the DJA and the locations of sources in the photometric catalogs, we make a pixel mask of the grid identifying which pixels do and do not have F444W coverage (hereafter referred to as the "edge mask").

B.1.2. Source Coordinate and Redshift Catalogs

Second, we produce a catalog of points to drop onto the grid. As the name suggests, this "source coordinate catalog" is just the R.A.′ and decl.′ coordinates of a subset of sources in the photometric catalog. Both UDS and EGS F444W reach 5σ depths at $\sim$28 mag, so first we remove all sources fainter than 27.5 mag in F444W. We require each source to have detections in at least three other bands, a fit photometric redshift ($z_{\rm phot} > -1$), and a photometry quality flag (USE_PHOT = 1). We find that 68,944 sources meet these criteria in the UDS and 29,052 in the EGS.

Next, we construct a redshift array to pair with the catalog of R.A.′ and decl.′ coordinates. For each source in the source coordinate catalog, we randomly sample its associated `eazyp`(z) distribution 100 times to draw 100 probabilistic redshifts. This produces an $N \times 100$ grid, where N is the number of selected sources. The majority of our sources are observed in imaging alone (i.e., they have only photometric redshifts), which is sufficient to identify particularly massive protostructures and inform a measure of the average galaxy density in the field (e.g., Figure 13 in Y.-K. Chiang et al. 2013). However, we wish to also detect less massive, smaller protostructures and map associated substructure.

The wealth of available spectroscopy in the UDS and EGS fields will help by increasing the precision of our density measurements. Many sources have entries in multiple spectroscopic catalogs, so we assign redshifts based on the following ranking: $z_{\rm spec,MSA}$, $z_{\rm spec,ground}$, $z_{\rm best,3DHST}$, and $z_{\rm phot}$. The treatment of galaxies with $z_{\rm phot}$ is described above; below, we detail how redshifts for the various $z_{\rm spec}$ categories are resampled.

$z_{spec,MSA}$. For galaxies with a NIRSpec MSA spectrum for which we measured a redshift, we instead replace the redshifts sampled from the photometric $p(z)$ with a set sampled from the spectroscopic $p(z)$ instead (see Section 2.2).

$z_{spec,ground}$. Uncertainties on galaxies from ground-based catalogs are not provided, so we resample redshifts from a Gaussian centered on $z_{\rm spec,ground}$ with a conservative width $\sigma_z = 0.001(1 + z_{\rm spec,ground})$. The values of the quality flags in the UDS VANDELS catalog correspond with the probability

of the given spectroscopic redshift being correct; we apply this scheme to our ground-based sample overall. For the highest quality flag (4 in VANDELS/Deeper than Deep, or 7 in MOSDEF), we treat the redshift as 100% correct and sample redshifts only from the spectroscopic $p(z)$. The quality flag tier (3 in VANDELS/Deeper than Deep, or 5 and 6 in MOSDEF) is assumed to be correct 95% of the time. For each of these sources, we perform 100 weighted coin flips (where the weight is set by the source's flag probability); we use the resampled $z_{\rm spec}$ when heads is thrown and the redshifts sampled from the photometric $p(z)$ distribution when the result is tails (i.e., we leave the redshift entry in the grid as-is). DEEP2/3 redshifts are sourced from the 3DHST catalog, which only retains sources with the highest quality flag (flag 4). UDS ground-based redshifts in the 3DHST come from archival data of various small spectroscopic programs, and are ungraded but treated as "robust." Though we restrict only to high-quality redshift flags in this work, loosening this requirement and applying the VANDELS probability schematic to the few poor-quality flags in the catalogs (e.g., 75% for flag 2, 50% for flag 1) leaves our conclusions unchanged.

$z_{spec,3dHST}$. Because of the relatively low resolution of the HST grism, sources with grism redshifts in the 3DHST catalog (referred to as $z_{\rm grism}$ therein) have larger uncertainties than typical spectroscopic redshifts. Fortunately, the catalog provides upper and lower 1σ and 2σ uncertainties, so we are able to statistically account for this intrinsic limitation. First, we perform a quality cut: For any source with upper or lower $\sigma_{z_{\rm spec}} > 0.0375(1 + z_{\rm spec})$ (roughly the 90th percentile of $\sigma_{z_{\rm spec}}$ values), we ignore its entry in the 3DHST catalog and default to redshifts sampled from the photometric $p(z)$. Sources which fail this typically have uncertainties consistent with confusion of a single line as either [O III] 5008 or Hα and are typically lower redshift than the range we sample here, so this choice has no effects on our results. Then, from the remaining sources with sufficiently precise $z_{\rm spec}$, we resample redshifts from an asymmetric Gaussian cumulative distribution function (CDF), where the Gaussian CDF above/below the median ($z_{\rm spec}$) has dispersion equal to the upper/lower 1σ uncertainties from the 3DHST catalog. Incorporating the given 2σ uncertainties into our statistical resampling of 3DHST redshifts has negligible results on our results, so we just use the 1σ uncertainties for simplicity.

B.2. Overdensity Mapping with MCVT

In this section, we explain the method of quantifying environment at a given redshift using our input data (the field grid, source coordinate catalog, and redshift catalogs). For a target redshift $z_{\rm slice}$, we identify members of the redshift slice by iterating over the redshift catalog. For each source, it is identified as a member of the redshift slice if the line-of-sight comoving separation between it and the slice's redshift is less than 5 cMpc (i.e., $|D_{\rm C,los}(z_{\rm slice}) - D_{\rm C,los}(z_{{\rm source},h})| < 5$ cMpc) in a given iteration (index h). This means that galaxies with broad $p(z)$ distributions, such as those with only a few bands of photometry, are unlikely to fall into the same redshift slice multiple times; galaxies with narrower $p(z)$ distributions, such as those with features falling in medium bands, will fall into the slice somewhat more frequently; and galaxies with extremely narrow $p(z)$s (e.g., sources with MSA spectra) will almost always fall in the slice.

Having selected the galaxies in a given 10 cMpc-wide slice of the field, we next correct for edge effects by filling in the region outside the field F444W footprint with mock galaxies. Using the field grid edge mask, we can estimate an average source density $\overline{\Sigma}^{h}_{\rm MCV\,T}(z_{\rm slice})$ within the field for the iteration. We then multiply this surface density by the area of the region outside the footprint to obtain the expected number of sources that would lie in this region m (not necessarily an integer). To account for the uncertainty of this estimate, we randomly sample an integer M from a Poisson distribution with expectation value m. We randomly distribute M galaxies across the field grid pixels that lie outside the F444W footprint.

While it is possible to infer a single expectation value of, e.g., a Poisson distribution from all 100 $\overline{\Sigma}^{h}_{\rm MCV\,T}(z_{\rm slice})$ measurements, doing so would result in less variance in the number of sources outside the footprint, which would result in less variance in density measurements for sources near the footprint edges. We opt for this approach to inflate uncertainties for these sources and better reflect the poor constraints on density measurements at the footprint edges.

Having assigned the locations of real galaxies within the footprint and fake galaxies without it, we proceed with the Voronoi tessellation. We partition the field grid by assigning each pixel at R.A.$'_i$, decl.$'_j$ to the galaxy, real or fake, nearest to it. All pixels associated with a given source are grouped together into a cell and are assigned a value equal to the inverse of the area of the cell. Thus, the values of all pixels i, j of the cell are simply the surface density, $\Sigma^{h,i,j}_{\rm MCV\,T}(z_{\rm slice})$.

Having successfully produced a surface-density map for iteration h, we save the grid of $\Sigma^{h,i,j}_{\rm MCV\,T}(z_{\rm slice})$ pixels and repeat the process for iteration $h + 1$. After 100 iterations, for each pixel i, j, we take the median across the index h of all 100 $\Sigma^{h,i,j}_{\rm MCV\,T}(z_{\rm slice})$ to be $\Sigma^{i,j}_{\rm MCV\,T}(z_{\rm slice})$. We also take the 84th and 16th percentile values of $\Sigma^{h,i,j}_{\rm MCV\,T}(z_{\rm slice})$ across index h to be the uncertainties on the surface density for pixel i, j. Typically, uncertainties from the stacked MCVT maps are around $\sim$0.2 dex, and we do not find evidence for any strong dependence on local structure (e.g., uncertainties do not vary significantly near overdense peaks versus out near the median density).

We refer to this method as MCVT, which is similar to VMC (e.g., B. C. Lemaux et al. 2018) but distinct in setup and execution. In Figure 4, we show a single iteration on the left and the stacked median on the right (in the online journal, an animation shows all iterations and the development of the median image). Red points denote the location of the redshift slice members for a given iteration, and the field grid pixels are colored (with arbitrary scaling) by their $\log \Sigma^{h,i,j}_{\rm MCV\,T}(z_{\rm slice})$ on the left (the individual iteration maps) and $\log \Sigma^{i,j}_{\rm MCV\,T}(z_{\rm slice})$ on the right (the stacked median map). White contours indicate the boundaries of the F444W footprint. As k progresses, structures that are not detectable in individual iteration maps begin to appear in the median image.

We then convert the MCVT surface density to a galaxy overdensity measure (sometimes called density contrast), $\delta^{i,j}_{\rm gal} = (\Sigma^{i,j}_{\rm MCV\,T} - \widetilde{\Sigma}^{\rm footprint}_{\rm MCV\,T})/\widetilde{\Sigma}^{\rm footprint}_{\rm MCV\,T}$, where $\widetilde{\Sigma}^{\rm footprint}_{\rm MCV\,T}$ is the median of $\Sigma^{i,j}_{\rm MCV\,T}$ for all i, j such that R.A.$'_i$, decl.$'_j$ lies inside the F444W footprint.

Appendix C
Overdensity Candidates

This appendix contains Table C1, which lists moderate-confidence overdensity peaks (detected as overdense, but lacking spectroscopically confirmed massive galaxies).

Table C1
Moderate-confidence Overdensity Peaks/Protogroup Candidates

ID	$z_{\rm Bary}$	R.A.$_{\rm Bary}$ (deg)	Decl.$_{\rm Bary}$ (deg)	$\log(M_{\rm Peak}/M_{\odot})$	Volume (cMpc^3)	$n_{\rm MM}$[a]	$n_{\rm spec}$[b]
UDS-cPeak-z3.2-1	3.198	34.313304	−5.221757	13.2	210	0	4
UDS-cPeak-z3.2-2	3.227	34.394101	−5.161605	13.0	128	1	5
UDS-cPeak-z3.5-1	3.500	34.425231	−5.139681	13.1	154	0	5
UDS-cPeak-z3.5-2	3.529	34.359051	−5.268542	13.3	299	0	6
UDS-cPeak-z3.7	3.703	34.460275	−5.164235	13.5	474	1	16
UDS-cPeak-z3.8	3.814	34.380599	−5.135172	13.3	273	0	7
UDS-cPeak-z4.1	4.155	34.478842	−5.155469	13.0	146	0	3
UDS-cPeak-z4.4	4.370	34.362546	−5.263976	13.2	212	0	4
UDS-cPeak-z5.0	4.956	34.378338	−5.257451	13.5	493	0	6
EGS-cPeak-z3.1	3.100	214.805939	52.798141	13.1	193	2	8
EGS-cPeak-z3.4	3.383	214.957124	52.924336	13.1	178	0	8
EGS-cPeak-z3.6	3.629	214.795105	52.776795	13.4	394	1	8
EGS-cPeak-z3.8-1	3.761	214.892476	52.921095	13.2	191	0	8
EGS-cPeak-z3.8-2	3.778	214.838412	52.782531	13.3	300	2	9
EGS-cPeak-z4.5	4.477	214.932044	52.936171	13.4	406	0	5
EGS-cPeak-z4.6	4.599	214.923324	52.909619	13.4	392	0	6
EGS-cPeak-z4.8	4.808	214.871101	52.875618	13.8	835	0	15
EGS-cPeak-z5.0	5.000	214.954421	52.844443	13.1	163	0	4

Notes. Same as Table 2, but for the moderate-confidence detections ($n_{\rm HM} = 0$ and $n_{\rm MM} < 3$). We label these as "candidate" overdensities.
[a] The number of moderate-mass galaxies with $10 \leqslant \log(M_*/M_{\odot}) < 10.5$ in candidate overdensity.
[b] The number of spectroscopically confirmed galaxies in the candidate overdensity.

ORCID iDs

Ian McConachie https://orcid.org/0000-0002-2446-8770
Anna de Graaff https://orcid.org/0000-0002-2380-9801
Michael V. Maseda https://orcid.org/0000-0003-0695-4414
Joel Leja https://orcid.org/0000-0001-6755-1315
Yunchong Zhang https://orcid.org/0000-0001-6454-1699
David J. Setton https://orcid.org/0000-0003-4075-7393
Rachel Bezanson https://orcid.org/0000-0001-5063-8254
Leindert A. Boogaard https://orcid.org/0000-0002-3952-8588
Gabriel Brammer https://orcid.org/0000-0003-2680-005X
Nikko J. Cleri https://orcid.org/0000-0001-7151-009X
Olivia R. Cooper https://orcid.org/0000-0003-3881-1397
Karl Glazebrook https://orcid.org/0000-0002-3254-9044
Rashmi Gottumukkala https://orcid.org/0000-0003-0205-9826
Jenny E. Greene https://orcid.org/0000-0002-5612-3427
Andy D. Goulding https://orcid.org/0000-0003-4700-663X
Michaela Hirschmann https://orcid.org/0000-0002-3301-3321
Gourav Khullar https://orcid.org/0000-0002-3475-7648
Ivo Labbe https://orcid.org/0000-0002-2057-5376
Jorryt Matthee https://orcid.org/0000-0003-2871-127X
Tim B. Miller https://orcid.org/0000-0001-8367-6265
Rohan P. Naidu https://orcid.org/0000-0003-3997-5705
Themiya Nanayakkara https://orcid.org/0000-0003-2804-0648
Erica J. Nelson https://orcid.org/0000-0002-7524-374X
Pascal A. Oesch https://orcid.org/0000-0001-5851-6649
Sedona H. Price https://orcid.org/0000-0002-0108-4176
Katherine A. Suess https://orcid.org/0000-0002-1714-1905
Bingjie Wang https://orcid.org/0000-0001-9269-5046
Katherine E. Whitaker https://orcid.org/0000-0001-7160-3632
Christina C. Williams https://orcid.org/0000-0003-2919-7495

References

Abadi, M. G., Moore, B., & Bower, R. G. 1999, MNRAS, 308, 947
Alonso, S., Mesa, V., Padilla, N., & Lambas, D. G. 2012, A&A, 539, A46
Astropy Collaboration, Price-Whelan, A. M., Lim, P. L., et al. 2022, ApJ, 935, 167
Astropy Collaboration, Price-Whelan, A. M., Sipőcz, B. M., et al. 2018, AJ, 156, 123
Astropy Collaboration, Robitaille, T. P., Tollerud, E. J., et al. 2013, A&A, 558, A33
Baker, W. M., Lim, S., D'Eugenio, F., et al. 2025a, MNRAS, 539, 557
Baker, W. M., Valentino, F., Lagos, C. D. P., et al. 2025b, A&A, 702, A270
Baldry, I. K., Glazebrook, K., Brinkmann, J., et al. 2004, ApJ, 600, 681
Balogh, M. L., & Morris, S. L. 2000, MNRAS, 318, 703
Balogh, M. L., Navarro, J. F., & Morris, S. L. 2000, ApJ, 540, 113
Barone-Nugent, R. L., Trenti, M., Wyithe, J. S. B., et al. 2014, ApJ, 793, 17
Behroozi, P., & Silk, J. 2018, MNRAS, 477, 5382
Blanton, M. R., Hogg, D. W., Bahcall, N. A., et al. 2003, ApJ, 594, 186
Boylan-Kolchin, M. 2023, NatAs, 7, 731
Brammer, G. 2023a, grizli, v1.9.11, Zenodo, doi:10.5281/zenodo.8370018
Brammer, G. 2023b, msaexp: NIRSpec analyis tools, Zenodo, doi:10.5281/zenodo.8319596
Brammer, G., & Valentino, F. 2025, The DAWN JWST Archive: Compilation of Public NIRSpec Spectra, Zenodo, doi:10.5281/zenodo.15472354
Brammer, G. B., van Dokkum, P. G., & Coppi, P. 2008, ApJ, 686, 1503
Brammer, G. B., Whitaker, K. E., van Dokkum, P. G., et al. 2009, ApJL, 706, L173
Bugiani, L., Belli, S., Park, M., et al. 2025, ApJ, 981, 25
Calzetti, D., Armus, L., Bohlin, R. C., et al. 2000, ApJ, 533, 682
Carnall, A. C. 2017, arXiv:1705.05165
Carnall, A. C., Cullen, F., McLure, R. J., et al. 2024, MNRAS, 534, 325
Carnall, A. C., McLure, R. J., Dunlop, J. S., et al. 2023, Natur, 619, 716
Chabrier, G. 2003, PASP, 115, 763
Champagne, J. B., Wang, F., Zhang, H., et al. 2025a, ApJ, 981, 113
Champagne, J. B., Wang, F., Yang, J., et al. 2025b, ApJ, 981, 114
Chartab, N., Mobasher, B., Darvish, B., et al. 2020, ApJ, 890, 7
Chiang, Y.-K., Overzier, R., & Gebhardt, K. 2013, ApJ, 779, 127
Chittenden, H. G., Glazebrook, K., Nanayakkara, T., et al. 2026, MNRAS, 547, stag474
Choi, J., Dotter, A., Conroy, C., et al. 2016, ApJ, 823, 102
Cochrane, R. K. 2025, MNRAS, 544, 1530
Conroy, C., & Gunn, J. E. 2010, ApJ, 712, 833
Conroy, C., Gunn, J. E., & White, M. 2009, ApJ, 699, 486
Cooper, M. C., Newman, J. A., Weiner, B. J., et al. 2007, MNRAS, 383, 1058

Cucciati, O., Lemaux, B. C., Zamorani, G., et al. 2018, A&A, 619, A49
Cutler, S. E., Robbins, L., Marchesini, D., et al. 2026, ApJL, 1008, L11
Cutler, S. E., Whitaker, K. E., Weaver, J. R., et al. 2024, ApJL, 967, L23
Darvish, B., Mobasher, B., Sobral, D., Scoville, N., & Aragon-Calvo, M. 2015, ApJ, 805, 121
de Graaff, A., Brammer, G., Weibel, A., et al. 2025b, A&A, 697, A189
de Graaff, A., Hviding, R. E., Naidu, R. P., et al. 2026, MNRAS, 551, stag1567
de Graaff, A., Rix, H. W., Carniani, S., et al. 2024, A&A, 684, A87
de Graaff, A., Setton, D. J., Brammer, G., et al. 2025a, NatAs, 9, 280
Donnan, C. T., McLure, R. J., Dunlop, J. S., et al. 2024, MNRAS, 533, 3222
Dotter, A. 2016, ApJS, 222, 8
Dressler, A. 1980, ApJ, 236, 351
Drinkwater, M. J., Gregg, M. D., & Colless, M. 2001, ApJ, 548, L139
Duan, Q., Conselice, C. J., Li, Q., et al. 2025, MNRAS, 540, 774
Edward, A. H., Balogh, M. L., Bahe, Y. M., et al. 2024, MNRAS, 527, 8598
Falcón-Barroso, J., Sánchez-Blázquez, P., Vazdekis, A., et al. 2011, A&A, 532, A95
Finkelstein, S. L., Bagley, M. B., Ferguson, H. C., et al. 2023, ApJL, 946, L13
Finkelstein, S. L., Leung, G. C. K., Bagley, M. B., et al. 2024, ApJL, 969, L2
Forrest, B., Lemaux, B. C., Shah, E., et al. 2023, MNRAS, 526, L56
Forrest, B., Lemaux, B. C., Shah, E. A., et al. 2024, ApJ, 971, 169
Fudamoto, Y., Helton, J. M., Lin, X., et al. 2026, ApJ, 1008, 217
Garilli, B., McLure, R., Pentericci, L., et al. 2021, A&A, 647, A150
Gatica, C., Demarco, R., Dole, H., et al. 2023, MNRAS, 527, 3006
Glazebrook, K., Nanayakkara, T., Schreiber, C., et al. 2024, Natur, 628, 277
Gunn, J. E., & J. Richard, I. G. 1972, ApJ, 176, 1
Hamadouche, M. L., Whitaker, K. E., Valentino, F., et al. 2026, arXiv:2602.02485
Harris, C. R., Millman, K. J., van der Walt, S. J., et al. 2020, Natur, 585, 357
Heintz, K. E., Watson, D., Brammer, G., et al. 2024, Sci, 384, 890
Helton, J. M., Sun, F., Woodrum, C., et al. 2024a, ApJ, 962, 124
Helton, J. M., Sun, F., Woodrum, C., et al. 2024b, ApJ, 974, 41
Hine, N. K., Geach, J. E., Alexander, D. M., et al. 2016, MNRAS, 455, 2363
Hung, D., Lemaux, B. C., Gal, R. R., et al. 2020, MNRAS, 491, 5524
Hung, D., Lemaux, B. C., Cucciati, O., et al. 2025, ApJ, 980, 155
Hunter, J. D. 2007, CSE, 9, 90
Huško, F., Lacey, C. G., & Baugh, C. M. 2022, MNRAS, 518, 5323
Hviding, R. E., de Graaff, A., Miller, T. B., et al. 2025, A&A, 702, A57
Ito, K., Tanaka, M., Valentino, F., et al. 2023, ApJL, 945, L9
Ito, K., Valentino, F., Farcy, M., et al. 2025, A&A, 697, A111
Ito, K., Valentino, F., Brammer, G., et al. 2026, A&A, 710, A364
Jespersen, C. K., Carnall, A. C., & Lovell, C. C. 2025, ApJL, 988, L19
Jian, H.-Y., Lin, L., & Chiueh, T. 2012, ApJ, 754, 26
Jin, S., Sillassen, N. B., Magdis, G. E., et al. 2024, A&A, 683, L4
joblib developers, T. 2025, joblib, v1.5.1, Zenodo, doi:10.5281/zenodo.15496554
Johnson, B., & Leja, J. 2017, Bd-J/Prospector: Initial Release, v0.1, Zenodo, doi:10.5281/zenodo.1116491
Johnson, B. D., Leja, J., Conroy, C., & Speagle, J. S. 2021, ApJS, 254, 22
Kakimoto, T., Tanaka, M., Onodera, M., et al. 2024, ApJ, 963, 49
Kakimoto, T., Tanaka, M., Ito, K., et al. 2026a, arXiv:2604.21007
Kakimoto, T., Tanaka, M., Ando, M., et al. 2026b, arXiv:2604.11942
Kalita, B. S., Daddi, E., D'Eugenio, C., et al. 2021, ApJL, 917, L17
Kauffmann, G., Heckman, T. M., White, D. M. S., et al. 2003, MNRAS, 341, 33
Kawinwanichakij, L., Glazebrook, K., Nanayakkara, T., et al. 2026, ApJ, 997, 29
Killi, M., Watson, D., Brammer, G., et al. 2024, A&A, 691, A52
Kriek, M., & Conroy, C. 2013, ApJ, 775, L16
Kriek, M., Shapley, A. E., Reddy, N. A., et al. 2015, ApJS, 218, 15
Kubo, M., Umehata, H., Matsuda, Y., et al. 2021, ApJ, 919, 6
Lagos, C. d. P., Valentino, F., Wright, R. J., et al. 2024, MNRAS, 536, 2324
Laporte, N., Zitrin, A., Dole, H., et al. 2022, A&A, 667, L3
Larson, R. B., Tinsley, B. M., & Caldwell, C. N. 1980, ApJ, 237, 692
Lehmer, B. D., Alexander, D. M., Geach, J. E., et al. 2009, ApJ, 691, 687
Leja, J., Carnall, A. C., Johnson, B. D., Conroy, C., & Speagle, J. S. 2019, ApJ, 876, 3
Leja, J., Johnson, B. D., Conroy, C., van Dokkum, P. G., & Byler, N. 2017, ApJ, 837, 170
Lemaux, B. C., Cucciati, O., Fèvre, O. L., et al. 2022, A&A, 662, A33
Lemaux, B. C., Fèvre, O. L., Cucciati, O., et al. 2018, A&A, 615, A77
Lepore, M., Mascolo, L. D., Tozzi, P., et al. 2024, A&A, 682, A186
Leung, H. H., Carnall, A. C., Taylor, E., et al. 2026, MNRAS, 549, stag827
Lin, X., Egami, E., Sun, F., et al. 2026, ApJ, 997, 207
Liu, S., Zheng, X. Z., Shi, D. D., et al. 2023, MNRAS, 523, 2422
Lotz, J. M., Papovich, C., Faber, S. M., et al. 2013, ApJ, 773, 154
Man, A., & Belli, S. 2018, NatAs, 2, 695
Mascolo, L. D., Saro, A., Mroczkowski, T., et al. 2023, Natur, 615, 809
Maseda, M. V., de Graaff, A., Franx, M., et al. 2024, A&A, 689, A73
Mathews, E. P., Leja, J., Speagle, J. S., et al. 2023, ApJ, 954, 132
McConachie, I., Antwi-Danso, J., Chang, W., et al. 2026, ApJ, 1002, 74
McConachie, I., Wilson, G., Forrest, B., et al. 2022, ApJ, 926, 37
McConachie, I., Wilson, G., Forrest, B., et al. 2025, ApJ, 978, 17
McGee, S. L., Balogh, M. L., Wilman, D. J., et al. 2011, MNRAS, 413, 996
Mei, S., Hatch, N. A., Amodeo, S., et al. 2023, A&A, 670, A58
Momcheva, I. G., Brammer, G. B., van Dokkum, P. G., et al. 2016, ApJS, 225, 27
Morishita, T., Roberts-Borsani, G., Treu, T., et al. 2023, ApJL, 947, L24
Muldrew, S. I., Hatch, N. A., & Cooke, E. A. 2015, MNRAS, 452, 2528
Muzzin, A., Marchesini, D., Stefanon, M., et al. 2013, ApJ, 777, 18
Nanayakkara, T., Glazebrook, K., Jacobs, C., et al. 2024, Sci. Rep., 14, 3724
Nanayakkara, T., Glazebrook, K., Schreiber, C., et al. 2025, ApJ, 981, 78
Napolitano, L., Castellano, M., Pentericci, L., et al. 2025, A&A, 693, A50
Newman, A. B., Chartab, N., Qezlou, M., et al. 2025, ApJ, 988, 48
Newman, A. B., Rudie, G. C., Blanc, G. A., et al. 2022, Natur, 606, 475
Newman, J. A., Cooper, M. C., Davis, M., et al. 2013, ApJS, 208, 5
Oke, J. B., & Gunn, J. E. 1983, ApJ, 266, 713
Omori, K. C., Bottrell, C., Walmsley, M., et al. 2023, A&A, 679, A142
Pan, R., Suess, K. A., Marchesini, D., et al. 2025, ApJL, 990, L24
Park, M., Conroy, C., Johnson, B. D., et al. 2025, ApJ, 994, 165
Puskás, D., Tacchella, S., Simmonds, C., et al. 2025, MNRAS, 540, 2146
Ramachandran, P., & Varoquaux, G. 2011, CSE, 13, 40
Remus, R.-S., Dolag, K., & Dannerbauer, H. 2023, ApJ, 950, 191
Sanchez-Blazquez, P., Peletier, R. F., Jimenez-Vicente, J., et al. 2006, MNRAS, 371, 703
Schreiber, C., Labbé, I., Glazebrook, K., et al. 2018, A&A, 611, A22
Setton, D. J., Khullar, G., Miller, T. B., et al. 2024, ApJ, 974, 145
Shah, E. A., Lemaux, B., Forrest, B., et al. 2024, MNRAS, 529, 873
Shen, L., Lemaux, B. C., Lubin, L. M., et al. 2021, ApJ, 912, 60
Shi, K., Toshikawa, J., Lee, K.-S., et al. 2021, ApJ, 911, 46
Shibuya, T., Ito, Y., Asai, K., et al. 2025, PASJ, 77, 21
Siegel, J. C., Setton, D. J., Greene, J. E., et al. 2025, ApJ, 985, 125
Sillassen, N. B., Jin, S., Magdis, G. E., et al. 2026, A&A, 706, A344
Skelton, R. E., Whitaker, K. E., Momcheva, I. G., et al. 2014, ApJS, 214, 24
Slob, M., Kriek, M., Beverage, A. G., et al. 2024, ApJ, 973, 131
Speagle, J. S. 2020, MNRAS, 493, 3132
Staab, P., Lemaux, B. C., Forrest, B., et al. 2024, MNRAS, 528, 6934
Strateva, I., Ivezić, Željko, Knapp, G. R., et al. 2001, AJ, 122, 1861
Sun, H., Wang, T., Daddi, E., et al. 2025, ApJL, 993, L49
Tanaka, M., Onodera, M., Shimakawa, R., et al. 2024, ApJ, 970, 59
Tang, M., Stark, D. P., Plat, A., et al. 2025, ApJ, 991, 217
Tomczak, A. R., Lemaux, B. C., Lubin, L. M., et al. 2017, MNRAS, 472, 3512
Travascio, A., Cantalupo, S., Tozzi, P., et al. 2025, A&A, 694, A165
Turner, C., Tacchella, S., D'Eugenio, F., et al. 2025, MNRAS, 537, 1826
Urbano Stawinski, S. M., Cooper, M. C., Forrest, B., et al. 2024a, OJAp, 7, 46
Urbano Stawinski, S. M., Cooper, M. C., Finkelstein, S. L., et al. 2024b, MNRAS, 528, 5624
Valentino, F., Brammer, G., Gould, K. M. L., et al. 2023, ApJ, 947, 20
van der Burg, R. F. J., Rudnick, G., Balogh, M. L., et al. 2020, A&A, 638, A112
van der Wel, A., Franx, M., van Dokkum, P. G., et al. 2014, ApJ, 788, 28
Vogt, F. P. A., Owen, C. I., Verdes-Montenegro, L., & Borthakur, S. 2016, ApJ, 818, 115
Wang, B., Leja, J., Bezanson, R., et al. 2023, ApJL, 944, L58
Wang, B., Leja, J., Labbé, I., et al. 2024, ApJS, 270, 12
Watson, C., Tran, K.-V., Tomczak, A., et al. 2019, ApJ, 874, 63
Weaver, J. R., Cutler, S. E., Pan, R., et al. 2024, ApJS, 270, 7
Weaver, J. R., Davidzon, I., Toft, S., et al. 2023, A&A, 677, A184
Weibel, A., Oesch, P. A., Barrufet, L., et al. 2024, MNRAS, 533, 1808
Wetzel, A. R., Tinker, J. L., & Conroy, C. 2012, MNRAS, 424, 232
Wright, L., Whitaker, K. E., Weaver, J. R., et al. 2024, ApJL, 964, L10
Xie, L., De Lucia, G., Fontanot, F., et al. 2024, ApJL, 966, L2
Zhang, Y., de Graaff, A., Setton, D. J., et al. 2026a, ApJ, 997, 252
Zhang, Y., Ji, Z., Bezanson, R., et al. 2026b, ApJL, 1004, L35